The Madden-Julian Oscillation in the Energy Exascale Earth System Model Version 1

Daehyun Kim[1], Daehyun Kang[2], Min-Seop Ahn[3], Charlotte DeMott[4], Chia-Wei Hsu[4], Changhyun Yoo[5], L. Ruby Leung[6], Samson Hagos[6], and Philip J. Rasch[f]

[1] Department of Atmospheric Sciences, University of Washington, Seattle, Washington

[2] Department of Oceanography, Chonnam National University, Gwangju, South Korea

[3] PCMDI, Lawrence Livermore National Laboratory, Livermore, California

[4] Department of Atmospheric Science, Colorado State University, Fort Collins, Colorado

[5] Department of Climate and Energy Systems Engineering, Ewha Womans University, Seoul, South Korea

[6] Pacific Northwest National Laboratory, Richland, Washington

Corresponding author: Daehyun Kim (daehyun@uw.edu)

Key Points:

- E3SMv1 simulates MJOs that exhibit realistic eastward propagation over the Indo-Pacific warm pool.
- Modelled processes of the MJO, revealed through column-integrated MSE anomalies, matches well with those in observation.
- Impact of the MJO on diurnal precipitation, MJO teleconnections to midlatitudes and interannual variability of the MJO are examined.

Abstract

The present study examines the characteristics of the MJO events represented in the Energy Exascale Earth System Model version 1 (E3SMv1), DOE's new Earth system model. The coupled E3SMv1 realistically simulates the eastward propagation of precipitation and Moist Static Energy (MSE) anomalies associated with the MJO. As in observation, horizontal moisture advection and longwave radiative feedback are found to be the dominant processes in E3SMv1 that lead to the eastward movement and maintenance of the MSE anomalies, respectively. Modulation of the diurnal cycle of precipitation in the Maritime Continent region by the MJO is also well represented in the model despite systematic biases in the magnitude and phase of the diurnal cycle. On the midlatitude impact of the MJO, E3SMv1 reasonably captures the pattern of the MJO teleconnection across the North Pacific and North America, with improvement in the performance in a high-resolution version, despite the magnitude being a bit weaker than the observed feature. About interannual variability of the MJO, the El Niño-Southern Oscillation (ENSO) modulation of the zonal extent of MJO's eastward propagation, as well as associated changes in the mean state moisture gradient in the tropical west Pacific, is well reproduced in the model. However, MJO in E3SMv1 exhibits no sensitivity to the Quasi-Biennial Oscillation (QBO), with the MJO propagation characteristics being almost identical between easterly QBO and westerly QBO years. Processes that have been suggested as critical to MJO simulation are also examined by utilizing recently developed process-oriented diagnostics.

Plain Language Summary

The United States Department of Energy developed a new computer model that simulates Earth's climate systems, called Energy Exascale Earth System Model version 1 (E3SMv1). This study examines how well the model reproduces the characteristics of the Madden-Julian Oscillation (MJO), a tropical climate phenomenon that impacts weather and climate around the globe. We find that the strength and eastward movement of the MJO is realistically represented in the model. Variability of water vapor and radiation are the dominant processes for the MJO simulation, which agrees well with the real-world observations. Despite some unrealistic features, E3SMv1 successfully simulates the impact of the MJO on tropical precipitation at shorter than daily time scale and on large-scale atmospheric circulation in the midlatitude. The model also exhibits realistic year-to-year changes in east-west expansion of the MJO by the El Niño-Southern Oscillation, while no noticeable changes can be detected when stratospheric wind reverses its direction over the equator in every 1 or 2 years.

1 Introduction

Extreme weather and climate events, such as landfalling tropical cyclones, cold surges, and droughts, present a significant threat to heavily populated areas and have profound socio-economic impacts on many economic sectors, including energy, agriculture, and water resource management. As the occurrence frequency of extreme events is expected to increase with greenhouse gas-induced global warming, it is challenging to develop mitigation strategies for future extreme events. At the heart of those efforts are short-term predictions and long-term projections of extreme events, whose accuracy and reliability depend strongly on the fidelity of the numerical models used to produce them.

As the dominant source of Earth system predictability at the intraseasonal time scale, the Madden-Julian oscillation (MJO) (Madden and Julian 1971, 1972) is a known driver of many types of extreme events all over the globe (Zhang 2013). Examples of the extreme events affected by the MJO include extreme rainfall (e.g., Jones and Carvalho 2012), flooding (e.g., Bond and Vecchi 2003), cold surges (e.g., Jeong et al. 2005), fire (e.g., Reid et al. 2012), lightning (e.g., Abatzoglou and Brown 2009), tornado (e.g., Thompson and Roundy 2013), and tropical cyclones (e.g., Klotzbach 2014), and atmospheric rivers (e.g., Zhou et al. 2021; Hagos et al. 2021b). Given the MJO's bold fingerprint on the location, frequency, and intensity of these extreme events, a realistic representation of the MJO is arguably a prerequisite for any numerical weather and climate models to accurately simulate the societally relevant extreme events.

The main goal of the present study is to examine the characteristics of the MJO and its teleconnections in the Energy Exascale Earth System Model version 1 (E3SMv1) (Golaz et al. 2019; Leung et al. 2020), a fully coupled Earth system model developed as part of the ongoing E3SM program (e3sm.org) of the U.S. Department of Energy. Despite recent collective efforts to evaluate the performance of the model (Leung et al. 2020 and references therein), its MJO simulation fidelity has been only briefly documented in Golaz et al. (2019), who showed that the eastward propagation of the MJO is realistically represented in the ocean-atmosphere coupled version of E3SMv1 (their Figure 22), in Caldwell et al. (2019), who briefly compared the MJO in E3SMv1 at low (~100km) and high (~25km) resolutions, and in Orbe et al. (2020), who compared the MJO among other modes of variability in six U.S. climate models including E3SMv1. Our study provides the first in-depth analysis of the MJO variability in E3SMv1 simulations.

While significant progress has been made in MJO modeling in the past few decades (readers are referred to Kim and Maloney 2017, and Jiang et al. 2020 for reviews on the history of MJO modeling), an accurate representation of the MJO and its teleconnections is still one of the most challenging tasks for many GCMs (Jiang et al. 2015; Ahn et al. 2017, 2020a; Wang et al. 2020a,b). A particular aspect of MJO variability that most contemporary GCMs struggle with is the poor representation of the MJO interaction with the islands in the Maritime Continent (MC). The MJO exhibits peculiar behaviors when it propagates across the MC region, with its propagation sometimes ceasing (e.g., Kim et al. 2014b; Feng et al. 2015; Zhang and Ling 2017; DeMott et al. 2018; Kerns and Chen 2020) and its convection detouring around the MC islands toward the summer hemisphere (e.g., Wang and Rui 1990; Wu and Hsu 2009; Kim et al. 2017). In many GCMs, MJO propagation is disrupted too frequently, suggesting that the 'barrier' effects of MC islands on the MJO are exaggerated (e.g., Ling et al. 2017). While the land-sea contrast (e.g., Sobel et al. 2010), the steep topography (e.g., Wu and Hsu 2009), the persistent diurnal cycle of precipitation in the MC islands (e.g., Hagos et al. 2016; Zhang and Ling 2017),

and the mean state moisture gradient on the eastern side of Sumatra and Borneo (e.g., Jiang et al. 2019) have all been suggested as key aspects of the MC that damp MJO variability there, the leading mechanisms through which the MC islands affect MJO convection remain elusive. Reviews on this topic can be found in Jiang et al. (2020) and Kim et al. (2021). To our knowledge, no study has systematically examined how well GCMs simulate the southward detouring of the MJO during boreal winter.

Another aspect of MJO variability that is poorly represented in GCMs is the year-to-year variability. While many studies have documented how observed MJO events are affected by the El Niño southern oscillation (ENSO) (e.g., Woolnough et al. 2000; Tam and Lau 2005; Pohl and Matthews 2007; Gushchina and Dewitte 2012, Wei and Ren 2019; Zhang and Han 2020; Kang et al. 2021) and the quasi-biennial oscillation (QBO) (Yoo and Son 2016; Son et al. 2017; Nishimoto and Yoden 2017; Zhang and Zhang 2018; Hendon and Abhik 2018; Martin et al. 2021b), understanding of the underlying mechanisms of MJO modulation by low-frequency modes remains incomplete. Despite the statistically robust QBO-MJO relationship present in observations, no existing GCM seems to be able to reproduce the observed QBO-MJO relationship (Lee and Klingaman 2018; Kim et al. 2020), even with a QBO signal given through nudging (Martin et al. 2021a). Richter et al. (2019) showed that E3SMv1 simulates a QBO with a periodicity and amplitude that are shorter and larger, respectively, than observed; nonetheless, it is worthwhile to investigate whether and how strongly the QBO modulation of the MJO is simulated in the model.

Careful examination of model simulations can provide useful insights not only into the mechanism of the phenomenon of interest but also into model biases at the process level. Recent efforts to develop process-oriented MJO simulation diagnostics have emphasized moisture-convection coupling (e.g., Kim et al. 2014a), the gross moist stability (e.g., Benedict et al. 2014), cloud-radiation feedback (e.g., Kim et al. 2015), and the horizontal gradient of mean moisture (Gonzalez and Jiang 2017; Jiang 2017; DeMott et al. 2019; Ahn et al. 2020a; Kang et al. 2020) as the processes that are crucial for a model to be able to generate MJO variability internally. Meanwhile, the moist static energy and moisture budget of the MJO in observations/reanalysis products have also been documented in detail (e.g., Maloney 2009; Kiranmayi and Maloney 2011; Kim et al. 2014b; Sobel et al. 2014; Ren et al. 2021). By focusing on phenomena that are directly affected by the parameterization schemes of deep convection, clouds, and radiation, the process-based diagnostics can offer insights as to whether and how the parameterizations need to be improved. These diagnostics can also help assess whether the model simulates the MJO for the correct reason.

In this study, we will analyze simulations made with E3SMv1 to investigate MJO propagation, the MJO MSE budget, MJO teleconnections to the mid-latitudes, the interaction of the MJO with the MC islands, and the MJO-ENSO and MJO-QBO relationships. Processes that have been suggested as critical to MJO simulation will be examined by utilizing recently developed process-oriented diagnostics, which can guide further model development.

The manuscript is organized as follows. The model simulations and the reference datasets are described in Section 2. The diagnostics used in the analysis are explained in Section 3. In Section 4, we present the result of performance- and process-based diagnosis of MJO variability in E3SMv1 simulations, which is followed by a summary and conclusions in Section 5.

2 Model and Data

2.1 Reference data

In this study, The National Oceanic and Atmospheric Administration (NOAA) daily interpolated Outgoing Longwave Radiation (OLR) product (Liebmann and Smith 1996) is used as a proxy for tropical convection. The rain rate is taken from the Tropical Rainfall Measuring Mission (TRMM) Multi-satellite Precipitation Analysis (TMPA). The TRMM dataset used in this study is the post-real-time data of version 7 (3B42), with a temporal resolution of 3 hours and spatial resolution of 0.25° × 0.25° (Huffman et al. 2007). For sea surface temperature (SST), the Hadley Centre Sea Ice and Sea Surface Temperature (Rayner et al. 2003) dataset is used.

Various atmospheric state variables and the turbulent and radiative fluxes at the lower and upper boundaries of the atmosphere are obtained from the fifth generation of the European Centre for Medium-Range Weather Forecasts (ECMWF) reanalysis (ERA5) product (Hersbach et al. 2020).

The AVHRR OLR and ERA5 data are obtained for the period 1979–2018, and the TRMM rain rate for 1998-2018. All data are interpolated onto a 2.5° longitude × 2.5° latitude horizontal grid. In this study, we primarily focus on boreal winter from November to April (NDJFMA) when the MJO and its teleconnection to the extratropics are most pronounced. As an exception to this, the interannual variability of the MJO is investigated in DJF (Section 4.6).

2.2 E3SM version 1

E3SMv1 has been developed from the Community Earth System Model version 1 (CESM1) and by including numerous changes in the atmosphere and by replacing ocean, sea ice, and land ice models, all based on the Model for Prediction Across Scales (MPAS) that uses spherical centroidal voronoi tessellations for multi-resolution modeling. The E3SMv1 atmosphere model (EAM, Rasch et al. 2019; Xie et al. 2018) is based on the Community Atmosphere Model version 5 (CAM5), but with updates to the cloud microphysics, shallow convection, aerosol, and turbulence parameterizations. The vertical resolution was more than doubled (30 to 72 levels) and model top raised to allow an improved treatment of the lower stratosphere relative to CAM5. With the release of E3SMv1 in April 2018 both the low resolution (LR, Golaz et al. 2019) and high resolution (HR, Caldwell et al. 2019) model versions, where the atmosphere model is applied at a grid spacing of ~100km and ~25km, respectively, are available. The LR and HR versions of the model use somewhat different parameter settings to optimize model fidelity in the two model configurations, so differences are not due solely to resolution. Readers are referred to Leung et al. (2020) and references therein for the overview of development of E3SM and the evaluation of its performance.

Three sets of coupled simulations made with E3SMv1 are analyzed in this study. The 5-member ensemble Historical (1850-2014) simulation conducted with LR E3SMv1, which is available from the CMIP6 archive, is used to investigate the interannual variability of the MJO (Section 4.6). While covering a long period (165 years) and thereby providing enough samples for the examination of year-to-year variability, not all variables needed for detailed process studies are available from the Historical simulation. By branching off from one ensemble member of the Historical ensemble simulation, we performed a 20-yr (1995-2014) simulation with LR E3SMv1 by saving many atmospheric variables and turbulent and radiative fluxes at the surface and the top of the atmosphere at a 6-hourly interval. In addition, a 20-yr (1957-1976) simulation (Balaguru et al. 2020) made with HR E3SMv1, as an extension of the 50-yr run reported by

Caldwell et al. (2019) with time-invariant 1950s forcing, is used. Note that the output from the 20-year simulations made with LR and HR E3SMv1 are our primary dataset for most diagnostics. For the MJO MSE budget and MJO process-oriented diagnostics, only LR E3SMv1 is examined.

Figure 1 shows the longitude-lag diagrams of equatorial (10°S–10°N), intraseasonal precipitation anomalies regressed onto the Indian Ocean (5°S–5°N, 85–95°E) reference timeseries from observations (Fig. 1a) and from the three model simulations (Figs. 1b-d). The observed eastward propagation of intraseasonal precipitation anomalies associated with the MJO (Fig. 1a) is reasonably reproduced in all E3SMv1 simulations used in this study (Figs. 1b-d). A feature that is worth noting is that the MJO signal in LR E3SMv1 is greater than observed in the MC region (110°-140°E), suggesting the MJO experiences a weaker MC barrier effect in the model than in the observations. Comparison with HR E3SMv1 indicates that employing a higher horizontal resolution did not improve the MJO simulation, consistent with Caldwell et al. (2019) based on comparison of the precipitation power spectra at low and high resolutions. HR E3SMv1 features a somewhat faster and weaker MJO propagation in the MC region (Fig. 1c). Lastly, MJO propagation characteristics are qualitatively similar between the 20-year (Fig. 1b) and the Historical ensemble simulations (Fig. 1d).

3 Diagnosis of MJO and its teleconnections

In this section, we provide brief descriptions of the specific diagnostics that are used in this study to examine processes associated with the MJO and MJO teleconnections.

3.1 MJO life-cycle composite

To extract the MJO signal from observations and model simulations, we use a method that is similar to that of Wheeler and Hendon (2004), which is often referred to as the MJO life-cycle composite. For each dataset of interest, we obtain the combined empirical orthogonal functions (CEOFs) of 15°S-15°N averaged, intraseasonal (20-100 day bandpass filtered) anomalies of OLR and zonal wind at 850 and 200-hPa. For model simulation data, the resulting two leading CEOFs are rotated to best match the pattern of the observed counterparts. Once the leading pair of CEOFs are obtained, the corresponding PCs are used to define the 'phase' and 'amplitude' of the MJO, following Wheeler and Hendon (2004). The MJO life-cycle composite can be constructed for any atmospheric field or flux variable by averaging intraseasonal anomalies of the variable for each MJO phase (total of 8 "Real-Time Multivariate MJO" (RMM) phases) with an amplitude threshold of 1.

3.2 MJO MSE budget

To examine the moistening process associated with the maintenance and propagation of the MJO, we use the intraseasonal, vertically-integrated MSE budget equation:

$$\left\langle \frac{\partial m}{\partial t} \right\rangle' = -\left\langle \vec{V} \bullet \nabla_h m \right\rangle' - \left\langle \omega \frac{\partial m}{\partial p} \right\rangle' + LH' + SH' + \langle LW \rangle' + \langle SW \rangle' + res_m \,, \qquad (1)$$

where m is MSE ($= C_p T + gz + L_v q$), C_p is the specific heat of dry air at constant pressure, g is the gravitational constant, L_v is the latent energy of vaporization, T, q, LH and SH are temperature, specific humidity, surface latent and sensible heat fluxes, respectively, and LW and SW are longwave and shortwave radiative heating rates, respectively. res_m is the budget residual, which is obtained by subtracting all RHS terms from MSE tendency. The prime

indicates an intraseasonal anomaly, and the angle brackets denote the mass-weighted vertical integral from the surface to 100 hPa. The MSE budget analysis has been used to examine the propagation and maintenance of the MJO in observations and model simulations (e.g., Maloney 2009; Kiranmayi and Maloney 2011; Andersen and Kuang 2012; Arnold et al. 2013; Kim et al. 2014b). The relative contribution of the individual MSE budget terms to the maintenance (S_m) and propagation (S_p) of MSE anomalies can be estimated by projecting them upon MSE anomalies and their tendencies (e.g., Andersen and Kuang 2012):

$$S_m(F) = \frac{\|F' \cdot M'\|}{\|M' \cdot M'\|}\ , \tag{2a}$$

$$S_p(F) = \frac{\|F' \cdot \partial M'/\partial t\|}{\|\partial M'/\partial t \cdot \partial M'/\partial t\|}\ , \tag{2b}$$

where F' and M' are column-integrated MSE budget terms and MSE anomaly, respectively, and ||A|| is the integral of variable A over the domain 60°-180°E, 20°S-10°N, and MJO phases 1-8 in the MJO life-cycle composite.

3.3 MJO teleconnections

The lagged life-cycle composite is used to analyze the evolution of mid-latitude circulation anomalies associated with the MJO. For example, for MJO phase 3, days with an active (i.e., amplitude > 1) MJO are defined as zero lag days, and the lagged composites are constructed by averaging 500-hPa geopotential height anomalies for the successive lag days without an MJO amplitude constraint. To obtain patterns and daily time series of the Pacific North American (PNA) teleconnection, we perform the Rotated Principal Component Analysis with daily 500-hPa geopotential height anomalies in the region between 0°N-90°N (Barnston and Livezey 1987; Feldstein 2000). In observations and E3SMv1, the PNA pattern emerges as the third and first leading modes, respectively (not shown). The PNA index is obtained by projecting the pattern onto the daily anomalies over the North Pacific and North America (0°-90°N, 150°E-30°W).

4 Results

4.1 Mean state

From a perspective in which the MJO is defined as fluctuations around the climatological seasonal cycle, it is reasonable to assume that the mean state would have profound impacts on the characteristics of the MJO. In fact, many processes associated with the propagation and maintenance of the MJO have been suggested to be strongly affected by various features of the mean state, such as the zonal extent of the mean westerly wind near the equator over the warm pool (e.g., Inness et al. 2001), gross moist stability (e.g., Benedict et al. 2014), and horizontal gradient of mean moisture (e.g., Gonzalez and Jiang 2017; Jiang 2017; DeMott et al. 2019; Ahn et al. 2020a, b; Kang et al. 2020). In this subsection, we focus on the mean state over the Indo-Pacific warm pool, which consists of two ocean basins - the Indian Ocean and the western Pacific - and the archipelago in between, where the convective signal associated with the MJO is most active.

Figure 2 shows that the mean precipitation, 850-hPa zonal wind and precipitable water are reasonably simulated in LR and HR E3SMv1, though there are some systematic biases in each field. In the Indian Ocean and west Pacific, both versions of E3SMv1 exhibit a positive and a negative precipitation bias on the western and eastern sides of the basins, respectively. As a

result, the zonal gradient of the mean precipitation across the Indian Ocean is weaker than observed, while the opposite is the case in the western Pacific. In the tropical Pacific, especially to the east of the dateline, the model exhibits wet biases in the subtropics that are straddling a dry bias near the equator. It is worthwhile to note that this pattern of precipitation bias is common to many CMIP6 models (e.g., Fig. 1c in Hagos et al. 2021a), suggesting that the bias is rooted in a systematic bias in the representation of moist physics (Hagos et al. 2021a). The mean westerly wind in the equatorial Indian Ocean is underestimated in LR E3SMv1, presumably due to the weaker-than-observed zonal gradient in the mean precipitation. On the contrary, the mean westerly wind is overestimated in the Maritime Continent (between 100°–140°E) in LR and HR E3SMv1, with positive and negative precipitation biases prevail on the eastern and western sides of the region, respectively.

The mean precipitable water (PW) bias pattern overall mimics that of the mean precipitation, with a dry bias prevailing in the Indo-Pacific warm pool area in both version of E3SMv1. It has been shown in Golaz et al. (2019) and Caldwell et al. (2019) that the LR and HR E3SMv1 exhibit a weak warm SST bias in many parts of the Indo-Pacific warm pool, suggesting that the dry bias likely stems from the bias in moist physics. The climatological meridional moisture gradient is steeper in LR E3SMv1 than in ERA5 in the central and eastern Indian Ocean, with the magnitude of the dry bias being larger in the off-equatorial area than near the equator. In contrast, the zonal gradient in the mean PW is underestimated in LR and HR E3SMv1 in the equatorial Indian Ocean. The role of the mean state moisture gradient, especially that of the meridional gradient, on the propagation of the MJO in E3SMv1 will be further discussed in Section 4.3.

4.2 MJO propagation characteristics

Figure 3 shows the MJO life-cycle composite (Section 3.1) of precipitation (shaded) and column MSE anomalies (contours) for eight MJO phases. For HR E3SMv1, only precipitation anomalies are shown because the 3-D variables required to calculate MSE are not available. The geographical distribution of MJO precipitation anomalies is reasonably represented in both versions of E3SMv1, although their magnitude is underestimated in HR H3SMv1. In observations, during phase 1, anomalously enhanced convection associated with positive column MSE anomalies is located in the western and central Indian Ocean. Dry conditions prevail over the MC region, except in Borneo and Sumatra islands, where both precipitation and column MSE show near-zero or slightly positive anomalies. LR and HR E3SMv1 successfully capture this ‘vanguard’ precipitation signal (Peatman et al. 2014) in the MC islands, although its magnitude and the zonal extent to the east are slightly overestimated.

The development of positive precipitation anomalies in the eastern Indian Ocean during MJO phases 2 and 3 in E3SMv1 is not as pronounced as in observations, possibly due to the dry bias in the mean state there (Figure 2). A branch of MJO-related anomalous convection in the equatorial western Pacific appears in phase 3 and matures in phase 4 in the observations. This development of enhanced convection in the western equatorial Pacific and subsequently along the intertropical convergence zone occurs mostly in the northern hemisphere. In LR E3SMv1, the corresponding precipitation anomalies develop earlier than in observations by about 1 MJO phase (~ 5–8 days), indicating that the stronger-than-observed vanguard effect is related to the early onset of convection in the northern branch.

Another branch of MJO-associated convection anomalies propagates more slowly and mostly to the south of the equator, which has been described as the 'detouring' signal around the MC islands (e.g., Wang and Rui 1990; Kim et al. 2017). This branch of anomalous convection reaches the western Pacific in phase 6 and matures in phase 7, about 3 phases (~ 15–24 days) later than its northern counterpart. LR and HR E3SMv1 capture remarkably well the propagation of the southern branch along the oceanic channel between the MC islands and Australia in phases 4 and 5 and the subsequent development of MJO convection along the south Pacific convergence zone in phases 6 and 7.

4.3 MJO MSE budget

Intraseasonal variability of column MSE is mainly governed by that of column water vapor in the tropics (Wolding et al. 2016). In Figure 3, it is shown that precipitation and column MSE anomalies are positively correlated with each other in observations and in LR E3SMv1, suggesting that useful insights into the propagation and maintenance of the MJO precipitation anomalies can be obtained by examining the column MSE budget. Figure 4 shows the MSE budget terms (Eq. 1) during MJO phases 2 and 3 in observations (left) and LR E3SMv1 (right), while the relative contribution of each budget term on the propagation and maintenance of MJO MSE anomalies are displayed in Figure 5.

By design, the MSE tendency term is 90 degrees out of phase with MSE anomalies, showing positive (i.e., moistening) and negative (i.e., drying) tendency to the east and west of positive MSE anomalies (1st row in Figure 4). In LR E3SMv1, the horizontal and vertical MSE advection terms contribute dominantly to the propagation of the MJO MSE anomalies (2nd and 3rd rows in Figure 4), closely mimicking the corresponding observations. It is worthwhile to note that the horizontal and vertical MSE advection terms appear to play a dominant role in different areas. Over the MC area, enhanced horizontal advection of MSE appears to the south of the MC islands, where the southern branch of MJO convection propagates (Figure 3). On the contrary, vertical MSE advection moistens the eastern part of the MC and the western equatorial Pacific, mostly north of 5°S, where the northern branch of MJO convection prevails in later phases.

In both observations and LR E3SMv1, column-integrated radiative heating anomalies and surface turbulent heat fluxes partly compensate for the tendency by the advection terms, thereby opposing the eastward movement of the MSE anomalies (4th and 5th rows in Figure 4). In E3SMv1, the magnitude of horizontal advection and surface latent heat flux anomalies to the south of the MC islands is larger than the observed.

Regarding the maintenance of the MJO MSE anomalies, the main balance is found between the two processes that are strongly tied to convection - vertical advection and longwave heating; longwave heating moistens columns with positive MSE anomalies (Kim et al. 2015; Wolding and Maloney 2016), while vertical advection exports MSE out of the columns (i.e., positive gross moist stability, Neelin and Held 1987). The opposing role of the processes is represented realistically in LR E3SMv1, although the model underestimates the magnitude of anomalous vertical MSE advection and longwave heating in the eastern Indian ocean, where MJO convection is weaker.

Figure 5 shows the relative contribution from each MSE budget term to the propagation of MSE anomalies, which is quantified through the pattern projection method (Eq. 2). Consistent with what Figure 4 indicates, the accelerating effect of horizontal advection and the dragging effect from latent heat flux feedback is somewhat overestimated in LR E3SMv1. The stabilizing role of

vertical MSE advection is weaker than observed, while MJO MSE anomalies are overly damped by latent heat flux anomalies. To understand the model-observation discrepancy in the MJO MSE budget, the vertical structure of vertical velocity, specific humidity, and zonal wind anomalies are examined (Figure 6). Also shown in Figure 6 are the corresponding MSE and LH anomalies. While the negative latent heat flux anomalies are located slightly to the east of positive MSE anomalies in both observations and in LR E3SMv1, they are larger in magnitude and overlap more strongly with positive MSE anomalies in LR E3SMv1, indicating a stronger dragging and damping effect (LHF in Figure 5). This difference can be understood in terms of how wind anomalies are distributed around MJO convection center. Compared to observations, the westerly anomalies to the west of MJO convection are weaker, and the areas of positive MSE anomalies are more strongly dominated by easterly anomalies in the model. The easterly anomalies reduce wind speed, and hence the latent heat flux, by acting upon the climatological westerlies in the region (Figure 2). Meanwhile, the magnitude of the vertical velocity anomalies in the areas with positive MSE anomalies in the model is about 30% weaker than the observed, explaining the weaker damping effect from vertical MSE advection. The model specific humidity anomalies are muted near 850-hPa level where enhanced convection is located, in sharp contrast to ERA5, likely contributing to the weaker-than-observed vertical velocity anomalies.

Overall, LR E3SMv1 skillfully captures the observed horizontal distribution of individual MSE budget terms as well as the relative contributions to the propagation and maintenance of MJO MSE anomalies. The results for the other MJO phases are similar (not shown).

4.4 Modulation of MC diurnal cycle by the MJO

Many recent observational and modeling studies focused on the role of the diurnal cycle of convection in the MC islands on the propagation of the MJO (e.g., Hagos et al. 2016; Zhang and Ling 2017). It was hypothesized that strong convection over the MC islands associated with the diurnal cycle could inhibit oceanic convection nearby and hence block MJO propagation (Zhang and Ling 2017). Because anomalous convection associated with the MJO develops mainly over water (Sobel et al. 2008, 2010), suppression of MC oceanic convection during MJO phases 3 and 4 could terminate an MJO event.

Figure 7 displays the amplitude and phase of the precipitation diurnal cycle in observations and in LR and HR E3SMv1. LR E3SMv1 shows the biases in the diurnal cycle of precipitation in the MC region that are common to many global climate models (Baranowski et al. 2019; Xie et al. 2019; Tang et al. 2021): it underestimates the amplitude of the diurnal cycle while the peak phase of the diurnal cycle occurs too early. The peak amplitude of the diurnal cycle in the model is less than 50% of what TRMM observations suggest. The weaker-than-observed diurnal cycle amplitude over MC islands might explain why the apparent MC damping effect on the MJO is less pronounced in LR E3SMv1 (Figure 1). The time of maximum diurnal precipitation occurs a few to several hours earlier in the model than in observations over water and the islands. It is worthwhile to mention the difference in phasing of the diurnal cycle between LR E3SMv1 (a coupled simulation, Figure 7e) and the control simulation made with LR EAMv1 (an uncoupled simulation; Figure 12b in Xie et al. 2019); the peak diurnal rain seems to occur a few hours later in LR E3SMv1 over the islands than in LR EAMv1. This might suggest that air-sea coupling or the mean state changes due to coupling could affect the diurnal cycle timing phase. It is also possible that the parameter tuning conducted before freezing the coupled version (Table 1 in Golaz et al. 2019) have affected the simulation of the diurnal cycle. The systematic bias in the

diurnal cycle amplitude is partly alleviated in HR E3SMv1, presumably because it better resolves the complex land-sea contrast and steep topography in the region (Figure 7).

Although still too weak, the diurnal cycle amplitude almost doubles in HR E3SMv1 when compared to the low-resolution version. HR E3SMv1 experiences more pronounced MJO MC barrier effect (Figure 1), possibly due to the stronger mean MC diurnal cycle. However, the peak phase of the diurnal cycle in HR E3SMv1 is even earlier than in LR E3SMv1, suggesting that factors other than grid size may affect the phasing of the diurnal cycle.

Despite the biases in the amplitude and phase of the diurnal cycle, LR and HR E3SMv1 reasonably capture the modulation of the diurnal cycle amplitude by the MJO (Figure 8), especially over relatively big islands (Borneo and New Guinea), with the diurnal cycle being enhanced when the MJO's main convection center is located in the Indian Ocean (phases 1-3) and western Maritime Continent (phase 4). As in observations, the enhancement of the diurnal cycle appears to contribute to the vanguard precipitation anomalies (Figure 3) in phases 1 and 2. Presumably due to the coarse horizontal resolution, the modulation of the diurnal cycle by the MJO is most pronounced in the center of the islands in LR E3SMv1, whereas in observations and, to a lesser degree in HR E3SMv1, it is most pronounced in the coastal areas in Sumatra, Java, and Borneo and over the entire island in Sulawesi and New Guinea, again showing the benefit of employing a finer grid spacing on resolving the diurnal cycle of precipitation in the region.

Figure 9 shows the average evolution of oceanic and land precipitation in the western Maritime Continent area (15°S-10°N, 100°-120°E) as functions of the local time and the MJO phase. The MJO affects the diurnal cycle of MC land and oceanic convection mostly by changing the amplitude of the diurnal cycle, whereas its impact on the phase of the diurnal cycle (i.e., the local time when the diurnal precipitation peaks) is minimal. That is, precipitation composites exhibit substantial changes in their strength by MJO phases while their peaks remain around the same local time. Figure 9 also shows that oceanic precipitation peaks during MJO phases 4 and 5 while land precipitation maxima take place about 1–2 phases earlier, with the ratio of oceanic to land precipitation being the largest at MJO phase 5.

4.5 MJO teleconnections

Observational evidence (e.g., Weickmann 1983) and theoretical understanding (e.g., Hoskins and Karoly 1981) of the MJO's influence on the extratropical circulation were established in the early '80s (reviews on this topic are available in Stan et al. 2017 and Jiang et al. 2020). The systematic fluctuations of mid-latitude circulation associated with the MJO are understood as the anomalous rotational flow excited by the MJO 'Rossby wave source' (Sardeshmukh and Hoskins 1988), which then propagate through the medium of the extratropical basic state as a stationary Rossby wave packet (Hoskins and Karoly 1981; Hoskins and Ambrizzi 1993).

Consistent with the theoretical understanding, modeling studies of MJO teleconnections emphasized both accurate representation of MJO diabatic heating (Yoo et al. 2015; Stan and Straus 2019) and realistic extratropical basic state (Henderson et al. 2017) as key aspects for GCMs to correctly capture the circulation changes associated with the MJO. Because the two factors – MJO variability and the mean state – often show tradeoffs with conventional cumulus parameterization schemes (Kim et al. 2011; Mapes and Neale 2011), modeling MJO teleconnection presents a challenging problem for any GCM. MJO teleconnections in the contemporary GCMs are often too strong, too persistent, and extended too far to the east (Wang

et al. 2020a). Also, for the MJO's modulation of the Pacific North America (PNA) pattern (e.g., Mori and Watanabe 2008), the latitudinal position, zonal extent, and intensity of the Pacific subtropical jet show some robust relationship with the skill scores for MJO teleconnection in the models (Wang et al. 2020b).

Figure 10 shows 500-hPa geopotential height (Z500) anomalies (shaded) for four selected MJO phases in observations (left), the LR (middle) HR (right) simulations, together with the mean state 300-hPa zonal wind (green contours). The geopotential height anomalies are averaged between 5-9 days after the days with a strong MJO signal (amplitude > 1). The Pacific subtropical jet is reasonably represented in both E3SMv1 simulations, although it is shifted slightly southward in LR E3SMv1, especially in the central Pacific. In observations, a negative and positive PNA pattern appears after MJO phases 3 and 7, respectively, which is realistically captured by both LR and HR E3SMv1 simulations. Interestingly, HR E3SMv1 seems to perform better in terms of the pattern and magnitude of MJO-associated Z500 anomalies, despite that precipitation anomalies associated with the MJO in HR E3SMv1 are weaker than in LR E3SMv1. The pattern correlations with the observed Z500 anomalies are overall higher in HR E3SMv1, except for the phase 1 result. The lead-lag relationship of PNA-like circulation anomalies with the MJO phases are also more realistically simulated in HR than in LR (Figure 11), suggesting that a finer grid spacing might be beneficial for a model to simulate the MJO teleconnections. For MJO phases 1 and 5, the observed Z500 anomalies are weaker than those for the other MJO phases (Tseng et al. 2019). The model-observation agreement is also low during phases 1 and 5 compared to that for phases 3 and 7, except for the eastern US for phase 5, in which HR E3SMv1 correctly captures the anomalous high.

4.6 Interannual variability of the MJO

We investigate in this subsection the modulation of MJO propagation characteristics by ENSO and QBO by utilizing the 5-member ensemble historical simulation made with LR E3SMv1. Note that the analysis in this subsection is limited to DJF.

4.6.1 ENSO-MJO

Many studies have examined how ENSO affects the MJO in the past few decades (e.g., (Slingo et al. 1999). In observations, MJO propagation tends to be damped more strongly over the MC region in La Niña years (e.g., Tam and Lau 2005; Gushchina and Dewitte 2012; DeMott et al. 2018; Wei and Ren 2019; Klingaman and DeMott 2020; Kang et al. 2021). Figure 12 shows that, to the east of around 110°E, the MJO OLR anomalies are much weaker during the La Niña years than in El Niño years. This contrast between El Niño and La Niña years is realistically captured in E3SMv1, showing that the MJO propagates farther to the east during the El Niño years.

Recent studies have emphasized the role of the mean state moisture gradient on the propagation of the MJO (e.g., DeMott et al. 2018; Klingaman and DeMott 2020; Kang et al. 2021). While detailed moisture budget analysis is not possible with the long-term historical simulation due to the unavailability of the required variables, Figure 13 offers clues on how the SST changes associated with ENSO can affect MJO variability. During El Niño years compared to La Niña years, the tropical Pacific Ocean experiences anomalously high SST near the equator and associated PW anomalies that are straddled by weaker cold SST and dry PW anomalies in the off-equatorial western and central Pacific. This pattern of PW anomalies steepens meridional gradient on both sides of the equator in the MC and west Pacific (Figure 13, second row). A steeper mean state meridional moisture gradient would lead to a larger meridional moisture

advection per unit meridional wind anomalies, promoting enhanced moisture recharging to the east of the MJO (Jiang 2017; DeMott et al. 2019; Ahn et al. 2020a; Ahn et al. 2020b; Kang et al. 2021). Also, the ENSO-associated PW anomalies weaken the climatological negative zonal moisture gradient in the western Pacific (Figure 13, third row). With the weaker negative zonal moisture gradient, the drying caused by MJO easterly anomalies to the east of MJO convection would be weaker during El Nino years compared to La Nina years, meaning that the basic state environment that is favorable for MJO is extended farther to the east. The E3SMv1 results support the notion that ENSO affects MJO by modulating the mean state moisture gradient.

4.6.2 QBO-MJO

Figure 14 compares MJO propagation characteristics between the easterly and westerly phases of QBO (EQBO and WQBO, respectively, hereafter). The propagation of the MJO during EQBO years is stronger and covers a wider zonal range than during WQBO years in observations (e.g., Yoo and Son 2016; Son et al. 2017). As in many other contemporary climate models, the MJO in E3SMv1 exhibits no sensitivity to the QBO, with MJO propagation characteristics being almost identical between EQBO and WQBO years (Figure 14), despite that the zonal mean temperature response to QBO in the upper troposphere and lower troposphere is realistically represented in E3SMv1 (Figure 15). We also examined the QBO-MJO relationship in the recent decades to see if the relationship emerges with the greenhouse gas-induced warming (Klotzbach et al. 2019). Our results showed that while the model could capture the lower stratospheric cooling in the recent decades, there was no notable trend in the QBO-MJO relationship (not shown). The lack of the QBO-MJO relationship in E3SMv1 might be due to the bias in the representation of the QBO, which is too fast and too strong compared to the observed QBO variability (Richter et al. 2019). Hendon and Abhik (2018) proposed a hypothesis that the zonal mean temperature anomaly associated with the QBO affects the MJO by modulating the strength of the cold cap above MJO convection. During EQBO years, the cold cap becomes stronger and provides enhanced positive feedback to anomalous convection, aiding further development. If the model convection scheme is not sensitive enough to the changes in the upper tropospheric and lower stratospheric static stability, it is possible that the parent model is unable to simulate the QBO-MJO relationship even with realistic representations of both.

4.7 Process-oriented MJO diagnostics

In this section, we present results from selected process-oriented MJO diagnostics that are designed to offer insights into the process-level bias of the model that may affect its MJO simulation fidelity. Many process-oriented MJO diagnostics focus on the moist thermodynamics in the atmosphere, in particular, the interaction among moisture, convection, cloud, and radiation. For the tropical oceans, the amount of rain over a large area is strongly tied to how saturated the column is (Bretherton et al. 2004; Peters and Neelin 2006; Rushley et al. 2018), which leads to a sharp contrast in rain rate between dry and wet columns. Kim et al. (2014) proposed the relative humidity composite based on precipitation (RHCP) diagnostic to quantify the strength of the coupling between moisture and precipitation. The RHCP diagnostic displays the lower free-tropospheric RH (average of 850- and 700-hPa RH) as a function of precipitation percentile. Figure 16a shows that the model RH is close to the reference (ERA5) overall, although slightly underestimated in the low precipitation percentiles. The precipitation-moisture coupling in the model measured as the RH difference between columns with high (upper 10%) and low (lower 20%) rain rate – the RHCP metric, which is shown to be positively correlated with MJO performance metrics (e.g., Kim et al. 2014; Jiang et al. 2015; Ahn et al. 2017) is

slightly weaker than in ERA5 (38.7% vs. 43.3%), suggesting that enhancing moisture sensitivity of convection in the model may lead to a stronger MJO (e.g., Kim et al. 2012).

The longwave cloud-radiation feedback has been suggested as the dominant maintenance mechanism of the MJO in many observational and model studies (e.g., Lin and Mapes 2004; Andersen and Kuang 2012; Sobel et al. 2014). One way of quantifying the strength of the longwave cloud-radiation feedback is by assessing the ratio between OLR and precipitation anomalies in the same unit, as an approximation to the ratio between anomalous column-integrated longwave and condensational heating. Figure 16b displays the ratio as a function of precipitation anomaly on a log scale, which is referred to as the Greenhouse Enhancement Factor (GEF) diagnostic in Kim et al. (2015). It was also shown in Kim et al. (2015) that the ratio for the weak-to-moderate rain rate anomalies (1–5 mm day^{-1}) – the GEF metric – exhibited a statistically significant positive correlation with MJO performance measures. LR E3SMv1 underestimates the GEF for precipitation anomalies lower than 3 mm day^{-1}, while overestimating it for higher intensity precipitation anomaly bins (Figure 16b). While the GEF metric from LR E3SMv1 is close to the reference value (0.26 vs. 0.3), the role of the weaker-than-observed GEF for the columns with weak precipitation anomalies on MJO variability in the model warrants further investigation.

The normalized gross moist stability (NGMS, Raymond et al. 2009) is a measure of how efficiently a column can export anomalous energy that goes into it through its boundaries (Neelin and Held 1987). It has been shown that models with a lower NGMS, hence less stable to energy input, tend to simulate stronger intraseasonal variability and MJO (e.g., Benedict et al. 2014). Ahn et al. (2017) estimated the NGMS as the ratio between column-integrated vertical MSE advection to column-integrated vertical dry static energy (DSE) advection using the time- and warm pool-averaged vertical profiles of MSE, DSE, and pressure velocity. They showed that the resulting NGMS metric is negatively correlated with MJO performance measure. Figures 16c show that warm pool averaged pressure velocity from LR E3SMv1 closely matches that from ERA5. In the MSE profile (Figure 16d), the overall shape is realistically captured in LR E3SMv1, despite the MSE value is lower than the observed throughout the troposphere associated with the dry bias (Figure 2). Nonetheless, the model NGMS obtained from the time- and warm pool-averaged profiles is close to the value from ERA5 (0.27 vs. 0.28), indicating that one metric – NGMS in this case – is not enough to characterize the simulated mean state. In the model development point of view, it will be of interest whether the dry bias can be alleviated without deteriorating the vertical profile of the mean MSE.

5 Summary and Conclusions

The Madden-Julian oscillation (MJO), the dominant source of Earth system predictability at the intraseasonal time scale, is a known driver of many types of extreme events all over the globe. However, an accurate representation of the MJO and its teleconnections is still one of the most challenging tasks for many global climate models (GCMs). In the current study, we documented the performance of the DOE's new Earth system model - the Energy Exascale Earth System Model version 1 (E3SMv1) in simulating MJO variability and its teleconnections. Simulations made with low (~100-km, LR) and high (~25-km, HR) resolution versions of E3SMv1 were analyzed with respect to their mean states (Section 4.1), MJO propagation characteristics (Section 4.2), MJO moist static energy (MSE) budgets (Section 4.3), MJO interactions with maritime continent (MC) islands (Section 4.4), MJO teleconnections to the mid-latitudes

(Section 4.5), and MJO regulation by interannual variability (Section 4.6). In addition, selected process-oriented MJO diagnostics were applied to the low-resolution E3SMv1 (Section 4.7).

We found that LR and HR E3SMv1 adequately simulate the eastward propagation of the MJO over the Indo-Pacific warm pool (Figure 1), despite that MJO convection anomalies are weaker in the Indian Ocean (Figure 3), which is presumably due to the bias in the mean state moisture (Figure 2). Interestingly, the widespread dry bias over the Indo-Pacific warm pool (Figure 2) does not severely affect the model's fidelity to simulate the eastward propagation of the MJO, suggesting either that the model mean state biases are not critical to MJO simulation or that the effect of the mean state bias is compensated by errors in other aspects of the model simulation.

It was shown that MJO precipitation anomalies in LR E3SMv1 were tightly coupled to column-integrated MSE anomalies (Figure 3), suggesting that moisture dynamics play a key role in their maintenance and propagation. The pattern and magnitude of individual MSE budget terms associated with the MJO in LR E3SMv1 closely mimic those in observations (Figures 4 and 5). The MSE budget highlighted that horizontal moisture advection, and longwave radiative feedback were key processes that led to the eastward movement and maintenance of MSE anomalies in the model, respectively. Despite our finding that the mean state zonal and meridional moisture gradient is weaker in the model than in observations (Figure 2), horizontal advection of MSE drives the MJO's eastward propagation more strongly in the model than in observations, due to the stronger-than-observed MJO wind anomalies in the model (Figure 5). On the other hand, the damping and dragging effects from latent heat flux feedback were found to be overestimated in the model, likely due to the bias in the wind-convection relationship (Figure 6). One contributing factor might be the underestimation of latent heat fluxes in the LR E3SMv1 surface flux parameterization in low wind conditions. This known deficiency has been partly alleviated in other versions of E3SM (e.g., Harrop et al, 2018) by using a "gustiness parameterization" that makes the surface fluxes sensitive to estimates of parameterized subgrid processes (convection, and turbulence).

The LR and HR E3SMv1 exhibited systematic biases in the magnitude and phase of the diurnal cycle of precipitation in the Maritime Continent (MC) region that are common to many other contemporary global climate models; the diurnal variation of precipitation was too weak, and it peaked a few to several hours earlier than observed (Figure 7). Despite the systematic biases, however, we found that the modulation of the diurnal cycle of precipitation in the MC region by the MJO was realistically captured in E3SMv1 (Figures 8 and 9), indicating that the model handles the interactions between large-scale MJO circulation and small-scale convective systems over the MC region in a realistic manner. The weak diurnal cycle over the MC islands in LR E3SMv1 might have contributed to the weaker-than-observed MC barrier effects on MJO (Figure 1), by facilitating the development of oceanic convection (Hagos et al. 2016; Zhang and Ling 2017).

The LR and HR E3SMv1 also reasonably captured the pattern and magnitude of circulation anomalies in the Pacific North America region while the magnitude was a bit weaker than the observed, especially for MJO phases 3 and 7 (Figure 10). On the other hand, the model representation of MJO teleconnection poorly matched the observed for MJO phases 1 and 5, when the teleconnection is relatively weak and less coherent in the PNA region. Interestingly, the HR E3SMv1 appeared to perform better than the low-resolution version in terms of the MJO-PNA relationship (Figure 11), suggesting that better resolving small-scale eddies in the mid-latitude might help improve MJO teleconnection.

As in observations, the zonal extent of the MJO's eastward propagation was strongly modulated by El Niño-Southern Oscillation (ENSO) in LR E3SMv1 (Figure 12). During El Niño years compared to La Niña years, the mean state moisture gradient in the tropical west Pacific changed to favor more effective moisture recharging by horizontal moisture advection to the east of MJO convection, facilitating further eastward propagation of MJO (Figure 13). Our results support recent observational and modeling studies that emphasized the role of the mean state moisture gradient as the critical feature of the mean state for the MJO's propagation.

On the contrary, LR E3SMv1, like many other contemporary global climate models, was found to be unable to capture the strong coupling between MJO and the stratospheric Quasi-Biennial Oscillation (QBO); MJO propagation characteristics showed no difference between the easterly QBO and westerly QBO years (Figure 14). The lack of the QBO-MJO coupling in E3SMv1, which realistically simulates the temperature changes associated with QBO in the upper troposphere and lower stratosphere (Figure 15), might suggest that the model convection and cloud parameterizations are missing an important process that is critical for convection to be sensitive to circulation changes in the upper troposphere and lower stratosphere. Another possibility is that the QBO influence on MJO variability is hindered because the model QBO oscillates too fast (Richter et al. 2019), making it difficult for the QBO-associated circulation changes to serve as the background conditions for MJO. Richter et al. (2019) showed that the bias in QBO periodicity and amplitude can be alleviated by tuning two key parameters in the gravity wave parameterization scheme. It will be of great interest to re-visit the MJO-QBO relationship in a future version of E3SM, in which the modified gravity wave parameterization will be implemented.

Aspects of the model simulation thought to be critical for MJO simulation were analyzed using recently developed process-oriented diagnostics. LR E3SMv1 slightly underestimates moisture-convection coupling (Figure 16a), particularly because the lower free-troposphere is not dry enough for the weak precipitation regimes (i.e., precipitation percentile < 40). Given that models tend to simulate a stronger MJO with a tighter moisture-convection coupling, our results suggest the possibility to improve MJO simulation fidelity in the model by enhancing the convection sensitivity to moisture. The longwave cloud-radiation feedback was found to be underestimated for weak precipitation anomalies (Figure 16b). Examining clouds in the weakly perturbed columns is warranted to improve the longwave cloud-radiation feedback, the main maintenance process for the MJO in the model (Figure 5). It was found that the vertical profiles of the mean state vertical velocity and moist static energy over the Indo-Pacific warm pool were realistically represented in LR E3SMv1 (Figures 16c and 16d), despite the dry bias throughout the troposphere, yielding the NGMS metric that is close to the observed. The good performance in the mean state overturning circulation likely contributed to the decent performance of the model in capturing MJO variability.

Collectively, our results have demonstrated that E3SMv1 is an excellent community tool to study the MJO and its associated extreme events in the current and future climates. As a follow-up study, we have been analyzing the modulation of tropical cyclones by MJO in the high-resolution E3SMv1 simulation, the results of which will be reported in a separate study.

667

668 **Acknowledgments**

669 D. Kim was supported by the DOE RGMA program (DE-SC0016223), the NOAA CVP program
670 (NA18OAR4310300), the NASA MAP program (80NSSC17K0227), and the Brain Pool
671 program funded by the Ministry of Science and ICT through the National Research Foundation
672 of Korea (NRF-2021H1D3A2A01039352). D. Kang was supported by Sejong Science
673 Fellowship funded by the National Research Foundation of Korea (NRF-
674 2021R1C1C2004621). Work of the LLNL-affiliated author (M.-S. Ahn) was performed under
675 the auspices of the U.S. Department of Energy by Lawrence Livermore National Laboratory
676 under Contract DE-AC52-07NA27344 and their efforts were supported by the Regional and
677 Global Model Analysis program area of the United States Department of Energy's Office of
678 Science. C. DeMott and C.-W. Hsu were supported by the DOE RGMA program (DE-
679 SC0020092). C. Yoo were supported by the National Research Foundation of Korea (NRF-
680 2018R1A6A1A08025520 and NRF-2019R1C1C1003161). R. Leung, S. Hagos, and P. Rasch
681 were also supported by the Office of Science of U.S. Department of Energy Biological and
682 Environmental Research as part of the Regional and Global Model Analysis program area.
683 PNNL is operated for the Department of Energy by Battelle Memorial Institute under contract
684 DE-AC05-76RL01830.

685

686 **Data Availability Statement**

687 The E3SM project, code, simulation configurations, model output, and tools to work with the
688 output are described at the website https://e3sm.org. Instructions on how to get started running
689 E3SM are available at the website https://e3sm.org/model/running-e3sm/e3sm-quick-start. All
690 model codes may be accessed on the GitHub repository (https://github.com/E3SM-
691 Project/E3SM). Model output data are accessible directly on NERSC or through the DOE Earth
692 System Grid Federation (https://esgf-node.llnl.gov/pro- jects/e3sm). The sources for various
693 observational data used in this study are as follows: TRMM precipitation
694 (https://gpm.nasa.gov/data/directory), ERA5 reanalysis
695 (https://www.ecmwf.int/en/forecasts/datasets/reanalysis-datasets/era5), NOAA daily interpolated
696 OLR (https://psl.noaa.gov/data/gridded/data.interp_OLR.html), and HadISST
697 (https://www.metoffice.gov.uk/hadobs/hadisst/).

698

699 **References**

700 Abatzoglou, J. T., and T. J. Brown, 2009: Influence of the Madden-Julian Oscillation on
701 Summertime Cloud-to-Ground Lightning Activity over the Continental United States. *Mon.*
702 *Weather Rev.*, **137**, 3596–3601, https://doi.org/10.1175/2009MWR3019.1.

703 Ahn, M.-S., D. Kim, K. R. Sperber, I.-S. Kang, E. Maloney, D. Waliser, and H. Hendon, 2017:
704 MJO simulation in CMIP5 climate models: MJO skill metrics and process-oriented diagnosis.
705 *Clim. Dyn.*, 1–23, https://doi.org/10.1007/s00382-017-3558-4.

706 ——, and Coauthors, 2020a: MJO Propagation Across the Maritime Continent: Are CMIP6
707 Models Better Than CMIP5 Models? *Geophys. Res. Lett.*, **47**, e2020GL087250,
708 https://doi.org/10.1029/2020GL087250.

709 ——, D. Kim, Y.-G. Ham, and S. Park, 2020b: Role of Maritime Continent Land Convection on
710 the Mean State and MJO Propagation. *J. Clim.*, **33**, 1659–1675, https://doi.org/10.1175/JCLI-
711 D-19-0342.1.

712 Andersen, J. A., and Z. Kuang, 2012: Moist Static Energy Budget of MJO-like Disturbances in
713 the Atmosphere of a Zonally Symmetric Aquaplanet. *J. Clim.*, **25**, 2782–2804,
714 https://doi.org/10.1175/JCLI-D-11-00168.1.

715 Arnold, N. P., Z. Kuang, and E. Tziperman, 2013: Enhanced MJO-like Variability at High SST.
716 *J. Clim.*, **26**, 988–1001, https://doi.org/10.1175/JCLI-D-12-00272.1.

717 Balaguru, K., and Coauthors, 2020: Characterizing Tropical Cyclones in the Energy Exascale
718 Earth System Model Version 1. *J. Adv. Model. Earth Syst.*, **12**, 1–23,
719 https://doi.org/10.1029/2019MS002024.

720 Baranowski, D. B., D. E. Waliser, X. Jiang, J. A. Ridout, and M. K. Flatau, 2019: Contemporary
721 GCM Fidelity in Representing the Diurnal Cycle of Precipitation Over the Maritime
722 Continent. *J. Geophys. Res. Atmos.*, **124**, 747–769, https://doi.org/10.1029/2018JD029474.

723 Barnston, A. G., and R. E. Livezey, 1987: Classification, seasonality and persistence of low-
724 frequency atmospheric circulation patterns. *Mon. Weather Rev.*, **115**, 1083–1126,
725 https://doi.org/10.1175/1520-0493(1987)115<1083:CSAPOL>2.0.CO;2.

726 Benedict, J. J., E. D. Maloney, A. H. Sobel, and D. M. W. Frierson, 2014: Gross Moist Stability
727 and MJO Simulation Skill in Three Full-Physics GCMs. *J. Atmos. Sci.*, **71**, 3327–3349,
728 https://doi.org/10.1175/JAS-D-13-0240.1.

729 Bond, N. A., and G. A. Vecchi, 2003: The Influence of the Madden–Julian Oscillation on
730 Precipitation in Oregon and Washington*. *Weather Forecast.*, **18**, 600–613,
731 https://doi.org/10.1175/1520-0434(2003)018<0600:TIOTMO>2.0.CO;2.

732 Bretherton, C. S., M. E. Peters, and L. E. Back, 2004: Relationships between water vapor path
733 and precipitation over the tropical oceans. *J. Clim.*, **17**, 1517-1528,
734 https://doi.org/10.1175/1520-0442(2004)017<1517:RBWVPA>2.0.CO;2

735 Caldwell, P. M., A. Mametjanov, Q. Tang, L. P. Van Roekel, J.-C. Golaz, J.-C., W. Lin, et al.,
736 2019: The DOE E3SM coupled model version 1: Description and results at high resolution.
737 *Journal of Advances in Modeling Earth Systems*, 11. https://doi.org/10.1029/2019MS001870.

738 ——, B. O. Wolding, E. D. Maloney, and D. A. Randall, 2018: Atmospheric Mechanisms for
739 MJO Decay Over the Maritime Continent. *J. Geophys. Res. Atmos.*, **123**, 5188–5204,
740 https://doi.org/10.1029/2017JD026979.

741 ——, N. P. Klingaman, W. L. Tseng, M. A. Burt, Y. Gao, and D. A. Randall, 2019: The
742 Convection Connection: How Ocean Feedbacks Affect Tropical Mean Moisture and MJO
743 Propagation. *J. Geophys. Res. Atmos.*, **124**, 11910–11931,
744 https://doi.org/10.1029/2019JD031015.

745 Feldstein, S. B., 2000: The timescale, power spectra, and climate noise properties of
746 teleconnection patterns. *J. Clim.*, **13**, 4430–4440, https://doi.org/10.1175/1520-
747 0442(2000)013<4430:TTPSAC>2.0.CO;2.

748 Feng, J., T. Li, and W. Zhu, 2015: Propagating and Nonpropagating MJO Events over Maritime
749 Continent. *J. Clim.*, **28**, 8430–8449, https://doi.org/10.1175/JCLI-D-15-0085.1.

750 Golaz, J. C., and Coauthors, 2019: The DOE E3SM Coupled Model Version 1: Overview and
751 Evaluation at Standard Resolution. *J. Adv. Model. Earth Syst.*, **11**, 2089–2129,
752 https://doi.org/10.1029/2018MS001603.

753 Gonzalez, A. O., and X. Jiang, 2017: Winter mean lower tropospheric moisture over the
754 Maritime Continent as a climate model diagnostic metric for the propagation of the Madden-
755 Julian oscillation. *Geophys. Res. Lett.*, **44**, 2588–2596,
756 https://doi.org/10.1002/2016GL072430.

757 Gushchina, D., and B. Dewitte, 2012: Intraseasonal Tropical Atmospheric Variability Associated
758 with the Two Flavors of El Niño. *Mon. Weather Rev.*, **140**, 3669–3681,
759 https://doi.org/10.1175/MWR-D-11-00267.1.

760 Hagos, S. M., C. Zhang, Z. Feng, C. D. Burleyson, C. De Mott, B. Kerns, J. J. Benedict, and M.
761 N. Martini, 2016: The impact of the diurnal cycle on the propagation of Madden-Julian
762 Oscillation convection across the Maritime Continent. *J. Adv. Model. Earth Syst.*, **8**, 1552–
763 1564, https://doi.org/10.1002/2016MS000725.

764 Hagos, S. M., L. R. Leung, O. A. Garuba, C. Demott, B. Harrop, J. Lu, and M.-S. Ahn, 2021a:
765 The Relationship between Precipitation and Precipitable Water in CMIP6 Simulations and
766 Implications for Tropical Climatology and Change. *J. Clim.*, **34**, 1587–1600,
767 https://doi.org/10.1175/JCLI-D-20-0211.1.

768 Hagos, S., L. R. Leung, O. Garuba, and C. M. Patricola, 2021b: Influence of background
769 divergent moisture flux on the frequency of North Pacific atmospheric rivers. *J. Clim*., 34,
770 6129-6139, doi:10.1175/jcli-d-21-0058.1.

771 Harrop, B. E., P. L. Ma, P. J. Rasch, R. B. Neale, and C. Hannay, 2018: The Role of Convective
772 Gustiness in Reducing Seasonal Precipitation Biases in the Tropical West Pacific. *J. Adv.*
773 *Model. Earth Syst.*, **10**, 961–970, https://doi.org/10.1002/2017MS001157.

774 Henderson, S. A., E. D. Maloney, and S.-W. Son, 2017: Madden–Julian Oscillation Pacific
775 Teleconnections: The Impact of the Basic State and MJO Representation in General
776 Circulation Models. *J. Clim.*, **30**, 4567–4587, https://doi.org/10.1175/JCLI-D-16-0789.1.

777 Hendon, H. H., and S. Abhik, 2018: Differences in Vertical Structure of the Madden-Julian
778 Oscillation Associated With the Quasi-Biennial Oscillation. *Geophys. Res. Lett.*, **45**, 4419–
779 4428, https://doi.org/10.1029/2018GL077207.

780 Hersbach, H., and Coauthors, 2020: The ERA5 global reanalysis. *Q. J. R. Meteorol. Soc.*, **146**,
781 1999–2049, https://doi.org/10.1002/qj.3803.

782 Hoskins, B. J., and D. J. Karoly, 1981: The Steady Linear Response of a Spherical Atmosphere
783 to Thermal and Orographic Forcing. *J. Atmos. Sci.*, **38**, 1179–1196,
784 https://doi.org/10.1175/1520-0469(1981)038<1179:TSLROA>2.0.CO;2.

785 ——, and T. Ambrizzi, 1993: Rossby Wave Propagation on a Realistic Longitudinally Varying
786 Flow. *J. Atmos. Sci.*, **50**, 1661–1671, https://doi.org/10.1175/1520-
787 0469(1993)050<1661:RWPOAR>2.0.CO;2.

788 Huffman, G. J., and Coauthors, 2007: The TRMM Multisatellite Precipitation Analysis (TMPA):
789 Quasi-global, multiyear, combined-sensor precipitation estimates at fine scales. *J.*
790 *Hydrometeorol.*, **8**, 38–55, https://doi.org/10.1175/JHM560.1.

791 Inness, P. M., J. M. Slingo, S. J. Woolnough, R. B. Neale, and V. D. Pope, 2001: Organization of
792 tropical convection in a GCM with varying vertical resolution; implications for the simulation
793 of the Madden-Julian Oscillation. *Clim. Dyn.*, **17**, 777–793,
794 https://doi.org/10.1007/s003820000148.

795 Jeong, J.-H., C.-H. Ho, B.-M. Kim, and W.-T. Kwon, 2005: Influence of the Madden-Julian
796 Oscillation on wintertime surface air temperature and cold surges in east Asia. *J. Geophys.*
797 *Res. Atmos.*, **110**, https://doi.org/https://doi.org/10.1029/2004JD005408.

798 Jiang, X., 2017: Key processes for the eastward propagation of the Madden-Julian Oscillation
799 based on multimodel simulations. *J. Geophys. Res. Atmos.*, **122**, 755– 770,
800 https://doi.org/10.1002/2016JD025955.

801 ——, and Coauthors, 2015: Vertical structure and physical processes of the Madden-Julian
802 oscillation: Exploring key model physics in climate simulations. *J. Geophys. Res. Atmos.*,
803 **120**, 4718–4748, https://doi.org/10.1002/2014JD022375.

804 ——, H. Su, and D. E. Waliser, 2019: A Damping Effect of the Maritime Continent for the
805 Madden-Julian Oscillation. *J. Geophys. Res. Atmos.*, **124**, 13693–13713,
806 https://doi.org/10.1029/2019JD031503.

807 ——, and Coauthors, 2020: Fifty Years of Research on the Madden-Julian Oscillation: Recent
808 Progress, Challenges, and Perspectives. *J. Geophys. Res. Atmos.*, **125**, e2019JD030911,
809 https://doi.org/https://doi.org/10.1029/2019JD030911.

810 Jones, C., and L. M. V Carvalho, 2012: Spatial-intensity variations in extreme precipitation in
811 the contiguous United States and the Madden-Julian oscillation. *J. Clim.*, **25**, 4898–4913,
812 https://doi.org/10.1175/JCLI-D-11-00278.1.

813 Kang, D., D. Kim, M.-S. Ahn, R. Neale, J. Lee, and P. J. Gleckler, 2020: The Role of the Mean
814 State on MJO Simulation in CESM2 Ensemble Simulation. *Geophys. Res. Lett.*, **47**,
815 e2020GL089824, https://doi.org/10.1029/2020GL089824.

816 ——, ——, ——, and S.-I. An, 2021: The Role of Background Meridional Moisture Gradient on
817 the Propagation of the MJO over the Maritime Continent. *J. Clim.*, 1–54,
818 https://doi.org/10.1175/JCLI-D-20-0085.1.

819 Kerns, B. W., and S. S. Chen, 2020: A 20-Year Climatology of Madden-Julian Oscillation
820 Convection: Large-Scale Precipitation Tracking From TRMM-GPM Rainfall. *J. Geophys.*
821 *Res. Atmos.*, **125**, 1–21, https://doi.org/10.1029/2019JD032142.

822 Kim, D., A. H. Sobel, E. D. Maloney, D. M. W. Frierson, and I.-S. Kang, 2011: A Systematic
823 Relationship between Intraseasonal Variability and Mean State Bias in AGCM Simulations. *J.*
824 *Clim.*, **24**, 5506–5520, https://doi.org/10.1175/2011jcli4177.1.

825 Kim, D., A. H. Sobel, A. D. Del Genio, Y. Chen, S. J. Camargo, M.-S. Yao, M. Kelley, and L.
826 Nazarenko, 2012: The Tropical Subseasonal Variability Simulated in the NASA GISS
827 General Circulation Model. *J. Clim.*, **25**, 4641–4659, https://doi.org/10.1175/JCLI-D-11-
828 00447.1.

829 ——, and Coauthors, 2014a: Process-Oriented MJO Simulation Diagnostic: Moisture Sensitivity
830 of Simulated Convection. *J. Clim.*, **27**, 5379–5395, https://doi.org/10.1175/JCLI-D-13-
831 00497.1.

832 ——, J.-S. Kug, and A. H. Sobel, 2014b: Propagating versus Nonpropagating Madden–Julian
833 Oscillation Events. *J. Clim.*, **27**, 111–125, https://doi.org/10.1175/JCLI-D-13-00084.1.

834 ——, M.-S. Ahn, I.-S. Kang, and A. D. Del Genio, 2015: Role of Longwave Cloud–Radiation
835 Feedback in the Simulation of the Madden–Julian Oscillation. *J. Clim.*, **28**, 6979–6994,
836 https://doi.org/10.1175/JCLI-D-14-00767.1.

837 ——, H. Kim, and M.-I. Lee, 2017: Why does the MJO detour the Maritime Continent during
838 austral summer? *Geophys. Res. Lett.*, **44**, 2579–2587, https://doi.org/10.1002/2017GL072643.

839 Kim, D. and E. D. Maloney, 2017: Review: Simulation of the Madden-Julian oscillation using
840 general circulation models, The Global Monsoon System, 3rd Edition, C.-P. Chang et al.,
841 Eds., 119-130.

842 Kim, D., E. D. Maloney, and C. Zhang, 2021: Review: MJO propagation over the Maritime
843 Continent, Chap. 21 in The Multiscale Global Monsoon System, Eds: C.P. Chang, K.J. Ha, R.
844 H. Johnson, D. Kim, G.N. Lau, B. Wang. World Scientific Series on Asia-Pacific Weather
845 and Climate, Vol. 11. World Scientific, Singapore, https://doi.org/10.1142/11723

846 Kim, H., J. M. Caron, J. H. Richter, and I. R. Simpson, 2020: The Lack of QBO-MJO
847 Connection in CMIP6 Models. *Geophys. Res. Lett.*, **47**, 1–8,
848 https://doi.org/10.1029/2020GL087295.

849 Kiranmayi, L., and E. D. Maloney, 2011: Intraseasonal moist static energy budget in reanalysis
850 data. *J. Geophys. Res. Atmos.*, **116**, D21117, https://doi.org/10.1029/2011JD016031.

851 Klingaman, N. P., and C. A. Demott, 2020: Mean State Biases and Interannual Variability Affect
852 Perceived Sensitivities of the Madden-Julian Oscillation to Air-Sea Coupling. *J. Adv. Model.*
853 *Earth Syst.*, **12**, 1–22, https://doi.org/10.1029/2019MS001799.

854 Klotzbach, P. J., 2014: The Madden–Julian Oscillation's Impacts on Worldwide Tropical
855 Cyclone Activity. *J. Clim.*, **27**, 2317–2330, https://doi.org/10.1175/JCLI-D-13-00483.1.

856 Klotzbach, P., S. Abhik, H. H. Hendon, M. Bell, C. Lucas, A. G. Marshall, and E. C. J. Oliver,
857 2019: On the emerging relationship between the stratospheric Quasi-Biennial oscillation and
858 the Madden-Julian oscillation. *Sci. Rep.*, **9**, 1–9, https://doi.org/10.1038/s41598-019-40034-6

859 Lee, J. C. K., and N. P. Klingaman, 2018: The effect of the quasi-biennial oscillation on the
860 Madden–Julian oscillation in the Met Office Unified Model Global Ocean Mixed Layer
861 configuration. *Atmos. Sci. Lett.*, **19**, 1–10, https://doi.org/10.1002/asl.816.

862 Leung, L. R., D. C. Bader, M. A. Taylor, and R. B. McCoy, 2020: An Introduction to the E3SM
863 Special Collection: Goals, Science Drivers, Development, and Analysis. *J. Adv. Model. Earth*
864 *Syst.*, **12**, https://doi.org/10.1029/2019MS001821.

Liebmann, C. A., and B. Smith, 1996: Description of a Complete (Interpolated) Outgoing Longwave Radiation Dataset. *Bull. Am. Meteorol. Soc.*, **77**, 1275–1277.

Lin, J. L., and B. E. Mapes, 2004: Radiation budget of the tropical intraseasonal oscillation. *J. Atmos. Sci.*, **61**, 2050–2062, https://doi.org/10.1175/1520-0469(2004)061<2050:RBOTTI>2.0.CO;2

Ling, J., C. Zhang, S. Wang, and C. Li, 2017: A new interpretation of the ability of global models to simulate the MJO. *Geophys. Res. Lett.*, **44**, 5798–5806, https://doi.org/10.1002/2017GL073891.

Madden, R. A., and P. R. Julian, 1971: Detection of a 40–50 Day Oscillation in the Zonal Wind in the Tropical Pacific. *J. Atmos. Sci.*, **28**, 702–708, https://doi.org/10.1175/1520-0469(1971)028<0702:DOADOI>2.0.CO;2.

——, and ——, 1972: Description of Global-Scale Circulation Cells in the Tropics with a 40–50 Day Period. *J. Atmos. Sci.*, **29**, 1109–1123, https://doi.org/10.1175/1520-0469(1972)029<1109:DOGSCC>2.0.CO;2.

Maloney, E. D., 2009: The Moist Static Energy Budget of a Composite Tropical Intraseasonal Oscillation in a Climate Model. *J. Clim.*, **22**, 711–729, https://doi.org/10.1175/2008JCLI2542.1.

Mapes, B., and R. Neale, 2011: Parameterizing Convective Organization to Escape the Entrainment Dilemma. *J. Adv. Model. Earth Syst.*, **3**, https://doi.org/10.1029/2011ms000042.

Martin, Z., C. Orbe, S. Wang, and A. Sobel, 2021a: The MJO-QBO Relationship in a GCM with Stratospheric Nudging. *J. Clim.*, 1–69, https://doi.org/10.1175/JCLI-D-20-0636.1.

——, S.-W. Son, A. Butler, H. Hendon, H. Kim, A. Sobel, S. Yoden, and C. Zhang, 2021b: The influence of the quasi-biennial oscillation on the Madden–Julian oscillation. *Nat. Rev. Earth Environ.*, **2**, 477–489 https://doi.org/10.1038/s43017-021-00173-9.

Mori, M., and M. Watanabe, 2008: The Growth and Triggering Mechanisms of the PNA: A MJO-PNA Coherence. *J. Meteorol. Soc. Japan. Ser. II*, **86**, 213–236, https://doi.org/10.2151/jmsj.86.213.

Neelin, J. D., and I. M. Held, 1987: Modeling tropical convergence based on the moist static energy budget. *Mon. Weather Rev.*, **115**, 3–12, https://doi.org/10.1175/1520-0493(1987)115<0003:MTCBOT>2.0.CO;2.

Nishimoto, E., and S. Yoden, 2017: Influence of the Stratospheric Quasi-Biennial Oscillation on the Madden–Julian Oscillation during Austral Summer. *J. Atmos. Sci.*, **74**, 1105–1125, https://doi.org/10.1175/JAS-D-16-0205.1.

Orbe, C., and Coauthors, 2020: Representation of modes of variability in six U.S. climate models. *J. Clim*., 33, 7591-7617, doi:10.1175/jcli-d-19-0956.1.

Peatman, S. C., A. J. Matthews, and D. P. Stevens, 2014: Propagation of the Madden–Julian Oscillation through the Maritime Continent and scale interaction with the diurnal cycle of precipitation. *Q. J. R. Meteorol. Soc.*, **140**, 814–825, https://doi.org/10.1002/qj.2161.

Peters, O., and J. Neelin, 2006: Critical phenomena in atmospheric precipitation. *Nat. Phys.*, **2**, 393–396, https://doi.org/10.1038/nphys314.

Pohl, B., and A. J. Matthews, 2007: Observed Changes in the Lifetime and Amplitude of the Madden–Julian Oscillation Associated with Interannual ENSO Sea Surface Temperature Anomalies. *J. Clim.*, **20**, 2659–2674, https://doi.org/10.1175/JCLI4230.1.

Rasch, P. J., and Coauthors, 2019: An Overview of the Atmospheric Component of the Energy Exascale Earth System Model. *J. Adv. Model. Earth Syst.* **11**, 2377–2411. https://doi.org/10.1029/2019MS001629.

Raymond, D. J., S. L. Sessions, A. H. Sobel, and Ž. Fuchs, 2009: The mechanics of gross moist stability. *J. Adv. Model. Earth Syst.*, **1**, https://doi.org/10.3894/JAMES.2009.1.9.

Rayner, N. A., D. E. Parker, E. B. Horton, C. K. Folland, L. V Alexander, D. P. Rowell, E. C. Kent, and A. Kaplan, 2003: Global analyses of sea surface temperature, sea ice, and night marine air temperature since the late nineteenth century. *J. Geophys. Res. Atmos.*, **108**, 4407, https://doi.org/10.1029/2002JD002670.

Reid, J. S., and Coauthors, 2012: Multi-scale meteorological conceptual analysis of observed active fire hotspot activity and smoke optical depth in the Maritime Continent. *Atmos. Chem. Phys.*, **12**, 2117–2147, https://doi.org/10.5194/acp-12-2117-2012.

Ren, P., D. Kim, M.-S. Ahn, D. Kang, and H.-L. Ren, 2021: Intercomparison of MJO Column Moist Static Energy and Water Vapor Budget among Six Modern Reanalysis Products. *J. Clim.*, **34**, 2977–3001, https://doi.org/10.1175/JCLI-D-20-0653.1.

Richter, J. H., C. C. Chen, Q. Tang, S. Xie, and P. J. Rasch, 2019: Improved Simulation of the QBO in E3SMv1. *J. Adv. Model. Earth Syst.*, **11**, 3403–3418, https://doi.org/10.1029/2019MS001763.

Rushley, S. S., D. Kim, C. S. Bretherton, and M.-S. Ahn, 2018: Reexamining thenonlinear moisture-precipitationrelationship over the tropical oceans. *Geophys. Res. Lett.*, **45**, 1133–1140, https://doi.org/10.1002/2017GL076296.

Sardeshmukh, P. D., and B. J. Hoskins, 1988: The Generation of Global Rotational Flow by Steady Idealized Tropical Divergence. *J. Atmos. Sci.*, **45**, 1228–1251, https://doi.org/10.1175/1520-0469(1988)045<1228:TGOGRF>2.0.CO;2.

Slingo, J. M., D. P. Rowell, K. R. Sperber, and F. Nortley, 1999: On the predictability of the interannual behaviour of the Madden-Julian oscillation and its relationship with el Niño. *Q. J. R. Meteorol. Soc.*, **125**, 583–609, https://doi.org/10.1002/qj.49712555411.

Sobel, A., S. Wang, and D. Kim, 2014: Moist Static Energy Budget of the MJO during DYNAMO. *J. Atmos. Sci.*, **71**, 4276–4291, https://doi.org/10.1175/JAS-D-14-0052.1.

Sobel, A. H., E. D. Maloney, G. Bellon, and D. M. Frierson, 2008: The role of surface heat fluxes in tropical intraseasonal oscillations. *Nat. Geosci*, **1**, 653–657.

——, ——, ——, and ——, 2010: Surface fluxes and tropical intraseasonal variability: A reassessment. *J. Adv. Model. Earth Syst.*, **2**, 2, https://doi.org/10.3894/JAMES.2010.2.2.

Son, S.-W., Y. Lim, C. Yoo, H. H. Hendon, and J. Kim, 2017: Stratospheric Control of the Madden–Julian Oscillation. *J. Clim.*, **30**, 1909–1922, https://doi.org/10.1175/JCLI-D-16-0620.1.

944 Stan, C., and D. M. Straus, 2019: The Impact of Cloud Representation on the Sub-Seasonal
945 Forecasts of Atmospheric Teleconnections and Preferred Circulation Regimes in the Northern
946 Hemisphere. *Atmosphere-Ocean*, **57**, 233–248,
947 https://doi.org/10.1080/07055900.2019.1590178.

948 ——, D. M. Straus, J. S. Frederiksen, H. Lin, E. D. Maloney, and C. Schumacher, 2017: Review
949 of Tropical-Extratropical Teleconnections on Intraseasonal Time Scales. *Rev. Geophys.*, **55**,
950 902–937, https://doi.org/10.1002/2016RG000538.

951 Tam, C.-Y., and N.-C. Lau, 2005: Modulation of the Madden-Julian Oscillation by ENSO:
952 Inferences from Observations and GCM Simulations. *J. Meteorol. Soc. Japan. Ser. II*, **83**,
953 727–743, https://doi.org/10.2151/jmsj.83.727.

954 Tang, S., P. Gleckler, S. Xie, J. Lee, M.-S. Ahn, C. Covey, and C. Zhang, 2021: Evaluating
955 Diurnal and Semi-Diurnal Cycle of Precipitation in CMIP6 Models Using Satellite- and
956 Ground-Based Observations. *J. Clim.*, 1–56, https://doi.org/10.1175/JCLI-D-20-0639.1.

957 Thompson, D. B., and P. E. Roundy, 2013: The Relationship between the Madden-Julian
958 Oscillation and U.S. Violent Tornado Outbreaks in the Spring. *Mon. Weather Rev.*, **141**,
959 2087–2095, https://doi.org/10.1175/MWR-D-12-00173.1.

960 Tseng, K.-C., E. Maloney, and E. Barnes, 2019: The Consistency of MJO Teleconnection
961 Patterns: An Explanation Using Linear Rossby Wave Theory. *J. Clim.*, **32**, 531–548,
962 https://doi.org/10.1175/JCLI-D-18-0211.1.

963 Wang, B., and H. Rui, 1990: Synoptic climatology of transient tropical intraseasonal convection
964 anomalies: 1975–1985. *Meteorol. Atmos. Phys.*, **44**, 43–61,
965 https://doi.org/10.1007/BF01026810.

966 Wang, J., H. Kim, D. Kim, S. A. Henderson, C. Stan, and E. D. Maloney, 2020a: MJO
967 Teleconnections over the PNA Region in Climate Models. Part I: Performance- and Process-
968 Based Skill Metrics. *J. Clim.*, **33**, 1051–1067, https://doi.org/10.1175/JCLI-D-19-0253.1.

969 ——, ——, ——, ——, ——, and ——, 2020b: MJO Teleconnections over the PNA Region in
970 Climate Models. Part II: Impacts of the MJO and Basic State. *J. Clim.*, **33**, 5081–5101,
971 https://doi.org/10.1175/JCLI-D-19-0865.1.

972 Wei, Y., and H. L. Ren, 2019: Modulation of ENSO on fast and slow MJO modes during boreal
973 winter. *J. Clim.*, **32**, 7483–7506, https://doi.org/10.1175/JCLI-D-19-0013.1.

974 Weickmann, K. M., 1983: Intraseasonal Circulation and Outgoing Longwave Radiation Modes
975 During Northern Hemisphere Winter. *Mon. Weather Rev.*, **111**, 1838–1858,
976 https://doi.org/10.1175/1520-0493(1983)111<1838:ICAOLR>2.0.CO;2.

977 Wheeler, M. C., and H. H. Hendon, 2004: An All-Season Real-Time Multivariate MJO Index:
978 Development of an Index for Monitoring and Prediction. *Mon. Weather Rev.*, **132**, 1917–
979 1932, https://doi.org/10.1175/1520-0493(2004)132<1917:AARMMI>2.0.CO;2.

980 Wolding, B. O., E. D. Maloney, and M. Branson, 2016: Vertically resolved weak temperature
981 gradient analysis of the Madden-Julian Oscillation in SP-CESM. *J. Adv. Model. Earth Syst.*,
982 **8**, 1586–1619, https://doi.org/10.1002/2016MS000724.

983 Woolnough, S. J., J. M. Slingo, and B. J. Hoskins, 2000: The Relationship between Convection
984 and Sea Surface Temperature on Intraseasonal Timescales. *J. Clim.*, **13**, 2086–2104,
985 https://doi.org/10.1175/1520-0442(2000)013<2086:TRBCAS>2.0.CO;2.

986 Wu, C.-H., and H.-H. Hsu, 2009: Topographic Influence on the MJO in the Maritime Continent.
987 *J. Clim.*, **22**, 5433–5448, https://doi.org/10.1175/2009JCLI2825.1.

988 Xie, S., and Coauthors, 2018: Understanding Cloud and Convective Characteristics in Version 1
989 of the E3SM Atmosphere Model. *J. Adv. Model. Earth Syst.*, **10**, 2618–44.
990 https://doi.org/10.1029/2018MS001350.

991 ——, and Coauthors, 2019: Improved diurnal cycle of precipitation in E3SM with a revised
992 convective triggering function. *J. Adv. Model. Earth Syst.*, **11**, 2290-2310.
993 https://doi.org/10.1029/2019MS001702.

994 Yoo, C., and S.-W. Son, 2016: Modulation of the boreal wintertime Madden-Julian oscillation by
995 the stratospheric quasi-biennial oscillation. *Geophys. Res. Lett.*, **43**, 1392–1398,
996 https://doi.org/10.1002/2016GL067762.

997 ——, S. Park, D. Kim, J.-H. Yoon, and H.-M. Kim, 2015: Boreal Winter MJO Teleconnection in
998 the Community Atmosphere Model Version 5 with the Unified Convection Parameterization.
999 *J. Clim.*, **28**, 8135–8150, https://doi.org/10.1175/JCLI-D-15-0022.1.

1000 Zhang, C., 2013: Madden–Julian Oscillation: Bridging Weather and Climate. *Bull. Am.*
1001 *Meteorol. Soc.*, **94**, 1849–1870, https://doi.org/10.1175/BAMS-D-12-00026.1.

1002 ——, and J. Ling, 2017: Barrier Effect of the Indo-Pacific Maritime Continent on the MJO:
1003 Perspectives from Tracking MJO Precipitation. *J. Clim.*, **30**, 3439–3459,
1004 https://doi.org/10.1175/JCLI-D-16-0614.1.

1005 ——, and B. Zhang, 2018: QBO-MJO Connection. *J. Geophys. Res. Atmos.*, **123**, 2957–2967,
1006 https://doi.org/10.1002/2017JD028171.

1007 Zhang, L., and W. Han, 2020: Barrier for the Eastward Propagation of Madden-Julian Oscillation
1008 Over the Maritime Continent: A Possible New Mechanism. *Geophys. Res. Lett.*, **47**, 1–12,
1009 https://doi.org/10.1029/2020GL090211.

1010 Zhou, Y., H. Kim, and D. E. Waliser, 2021: Atmospheric river lifecycle responses to the
1011 Madden-Julian Oscillation. *Geophys. Res. Lett.*, 48, e2020GL090983.
1012 https://doi.org/10.1029/2020GL090983

1013
1014

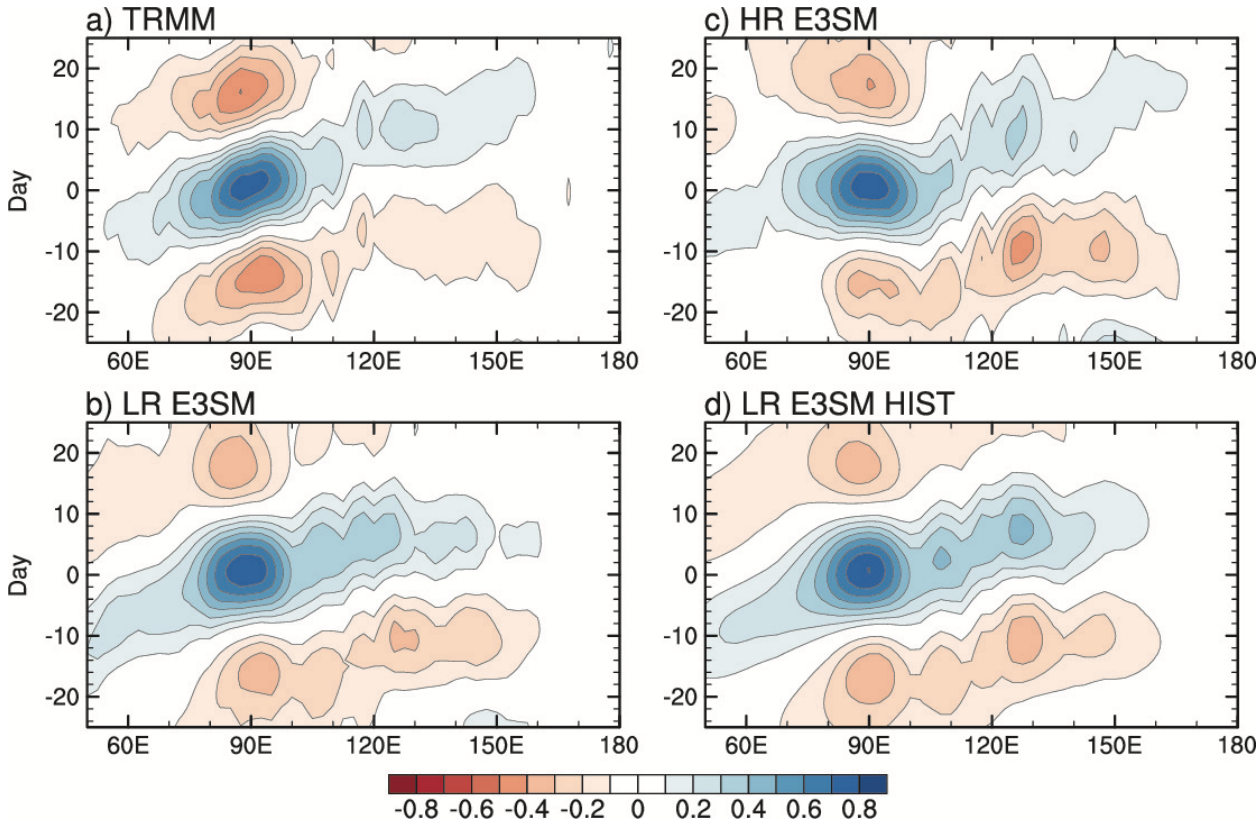

Figure 1. Longitude–lag diagram of equatorial (10°S–10°N) precipitation regressed against intraseasonal precipitation anomalies in the Indian Ocean reference region (5°S–5°N, 85–95°E) during NDJFMA for (a) TRMM and (b)-(d) E3SMv1 model simulations. For (b) and (c) LR and HR simulations of a recent 20-year period are used, while for (d) the 5-ensemble CMIP6 Historical simulation (1850-2014) made with LR E3SMv1 is used.

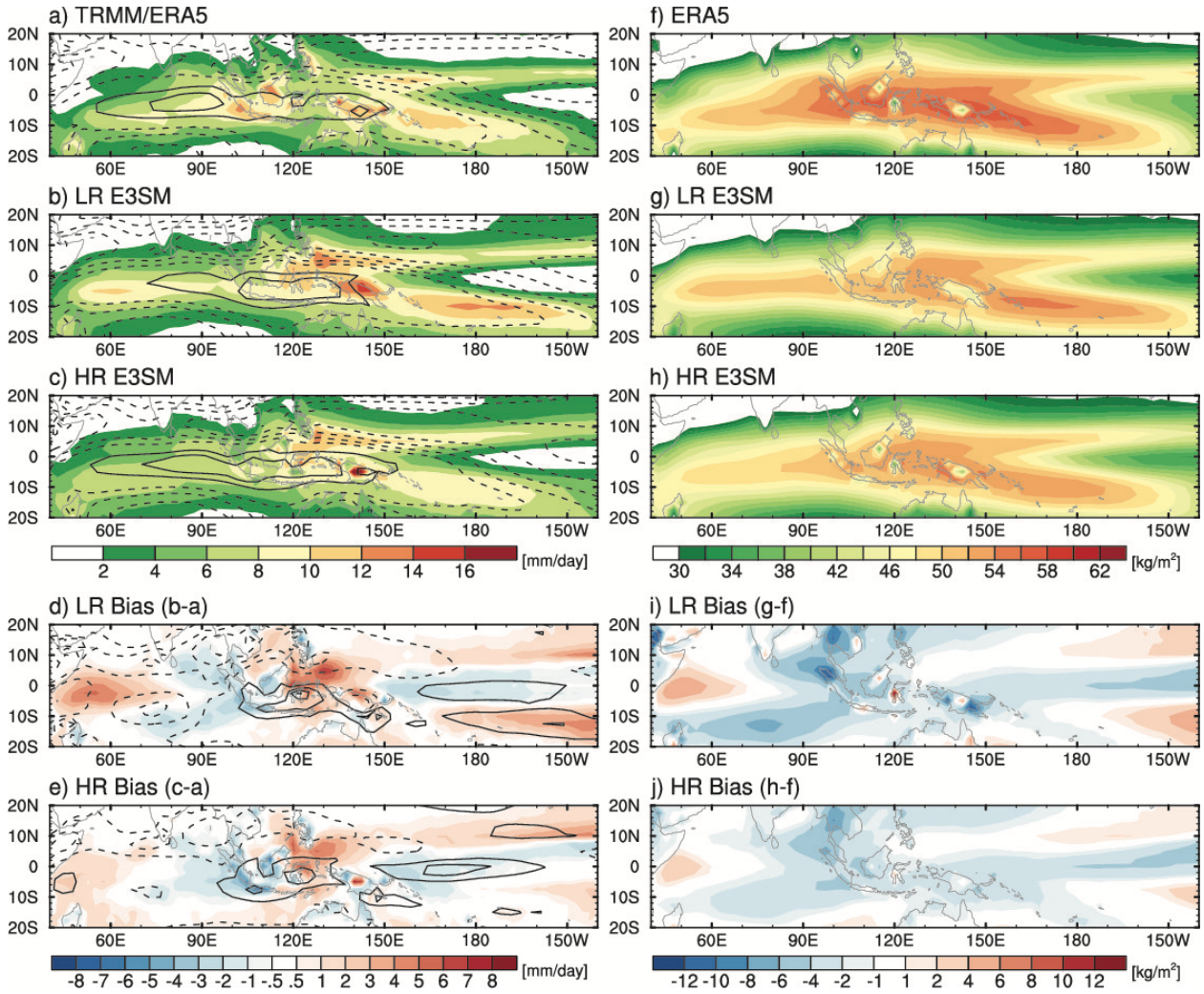

Figure 2. November-April mean state of (a, b, and c) precipitation (mm day^{-1}, shaded) and 850-hPa zonal wind (m s^{-1}, contour), and (f, g, and h) precipitable water (kg m^{-2}, shaded). The top three panels show observations, LR E3SMv1, and HR E3SMv1, respectively, while the bottom two row show the biases in LR E3SMv1 and HR E3SMv1, respectively. The contour interval for 850-hPa zonal wind is 2 m s^{-1}. For the bias, the contour intervals are 1 m s^{-1} for 850-hPa zonal wind and the zero lines are omitted.

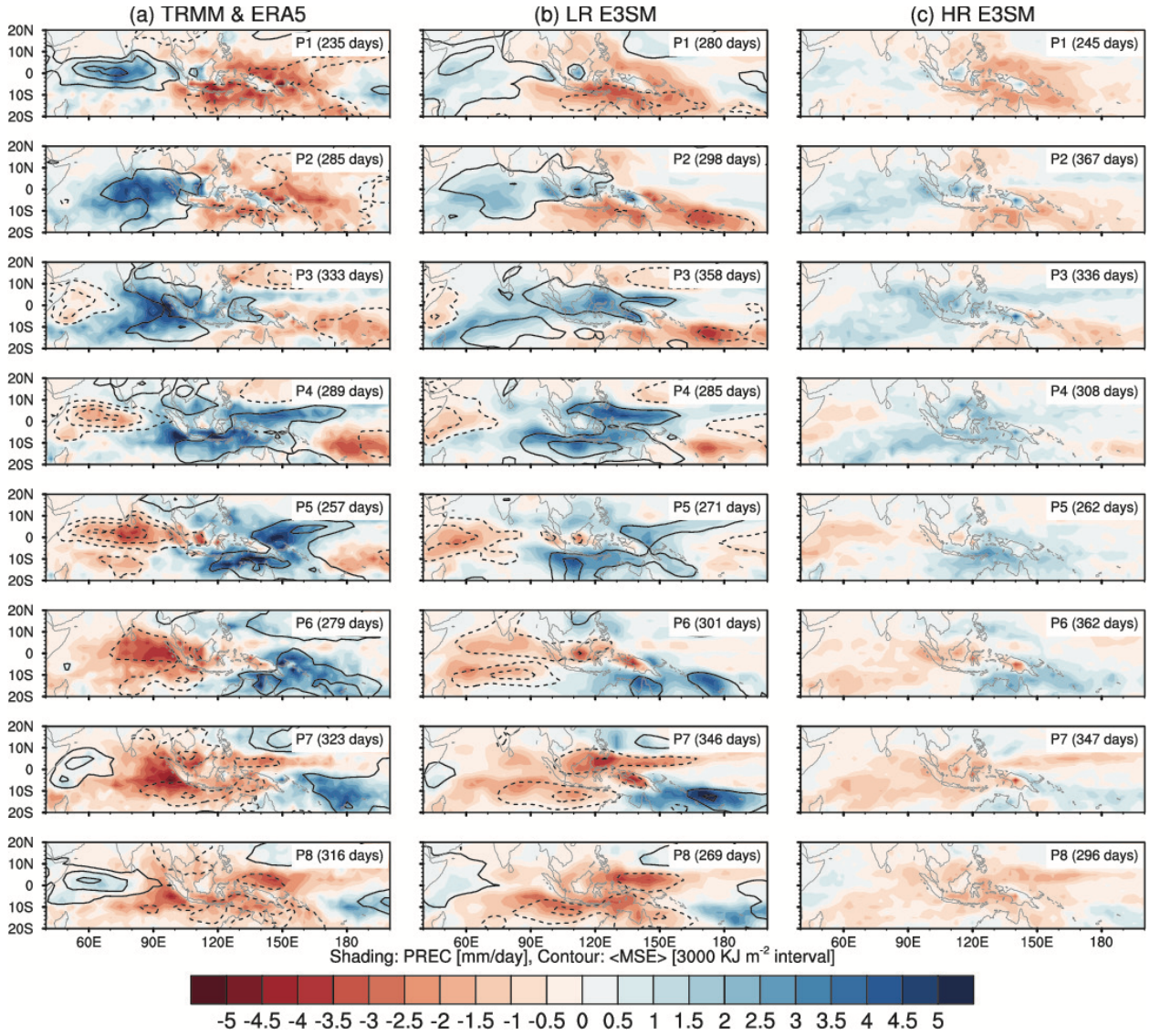

Figure 3. MJO life cycle composite maps of intraseasonal precipitation (mm day^{-1}, shaded) and column-integrated MSE anomalies (kJ m^{-2}, contour) obtained from each RMM phase (RMM amplitude > 1) during NDJFMA: a) observations, b) LR E3SMv1, and c) HR E3SMv1. The contour interval for column-integrated MSE anomalies is 3000 KJ m^{-2}. The number of days used in each phase composite is indicated in the parentheses.

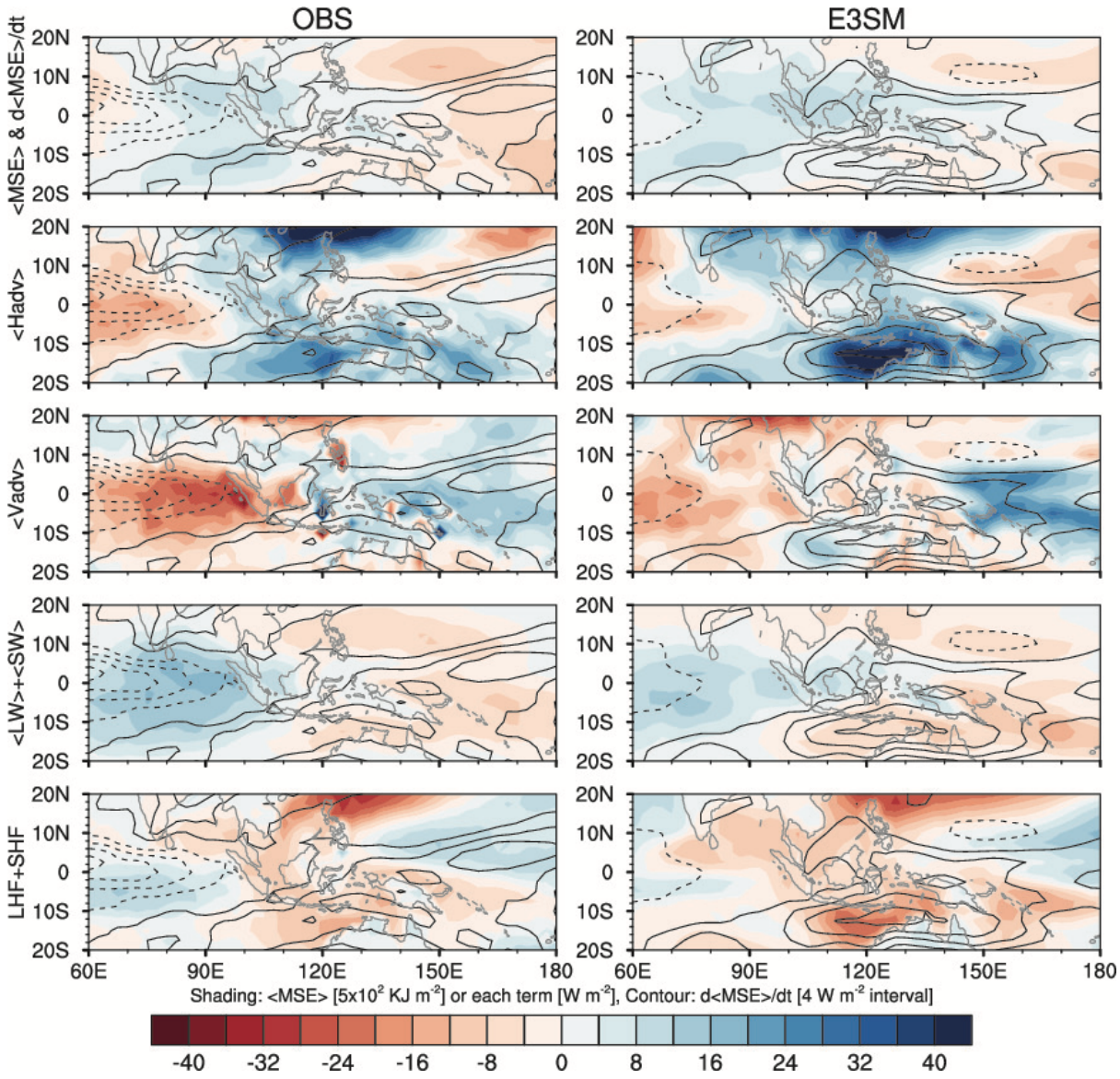

Figure 4. (1st row) Column-integrated MSE anomalies (kJ m^{-2}, shaded) and total MSE tendency (kJ m^{-2}, contour) composited for MJO phases 2 and 3: (left) ERA5 and (right) LR E3SMv1. (2nd to 5th rows) Same as the 1st row, except that shading indicates horizontal advection, vertical advection, radiative heating, and surface turbulent fluxes, respectively. The contour interval for total MSE tendency is 4 W m^{-2}.

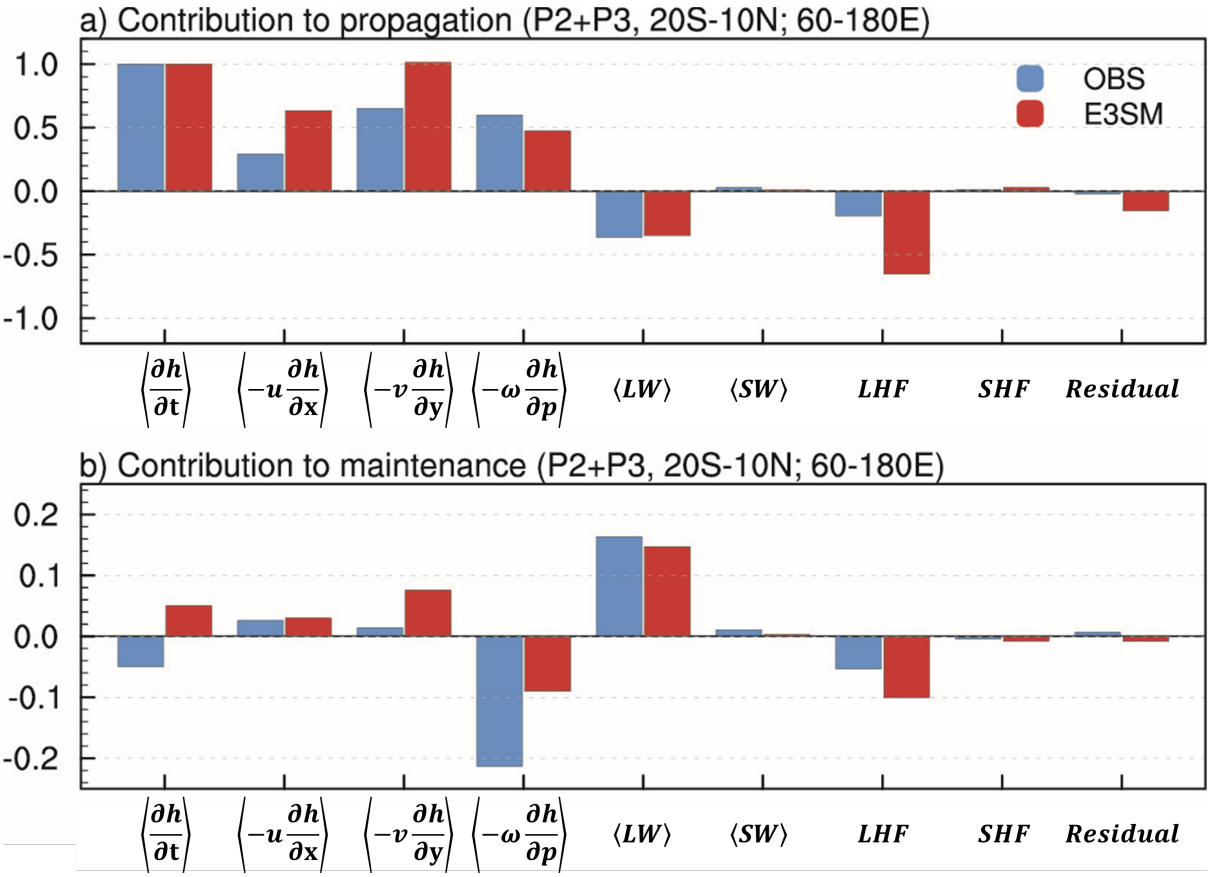

Figure 5. Contribution of each MSE budget term to the (a) propagation and (b) maintenance of the MJO during RMM phases 2 and 3 over the Indo-Pacific warm pool (20°S–10°N and 60–180°E) during NDJFMA. Blue and red bars indicate results from observations and E3SMv1, respectively.

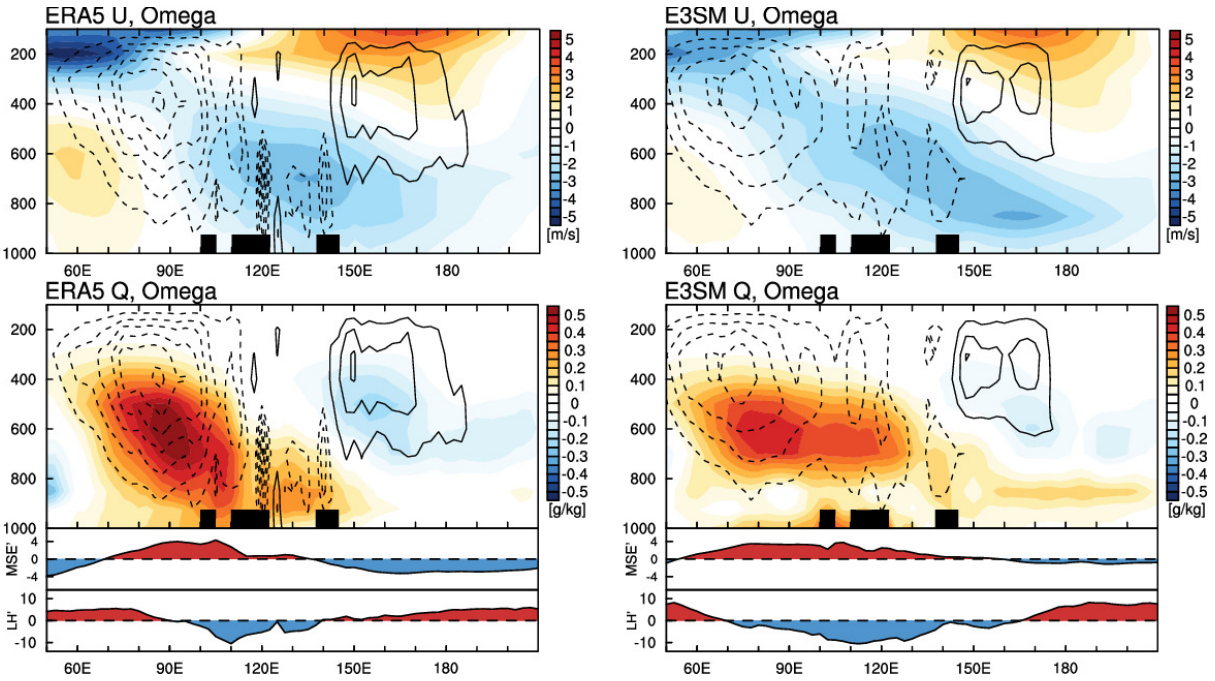

Figure 6. (top) Intraseasonal zonal wind (shaded, m s^{-1}) and pressure velocity (contour, Pa s^{-1}) anomalies averaged over the equatorial band (10°S-10°N) composited for MJO phases 2 and 3: (left) ERA5 and (right) LR E3SMv1. (bottom) Same as the top panels, except for intraseasonal specific humidity anomalies (g kg^{-1}) are shaded. The contour interval for pressure velocity is 0.005 Pa s^{-1}. Line graphs at the bottom indicate column-integrated intraseasonal MSE (x 10^4 kJ m^{-2}) and latent heat flux (W m^{-2}) anomalies.

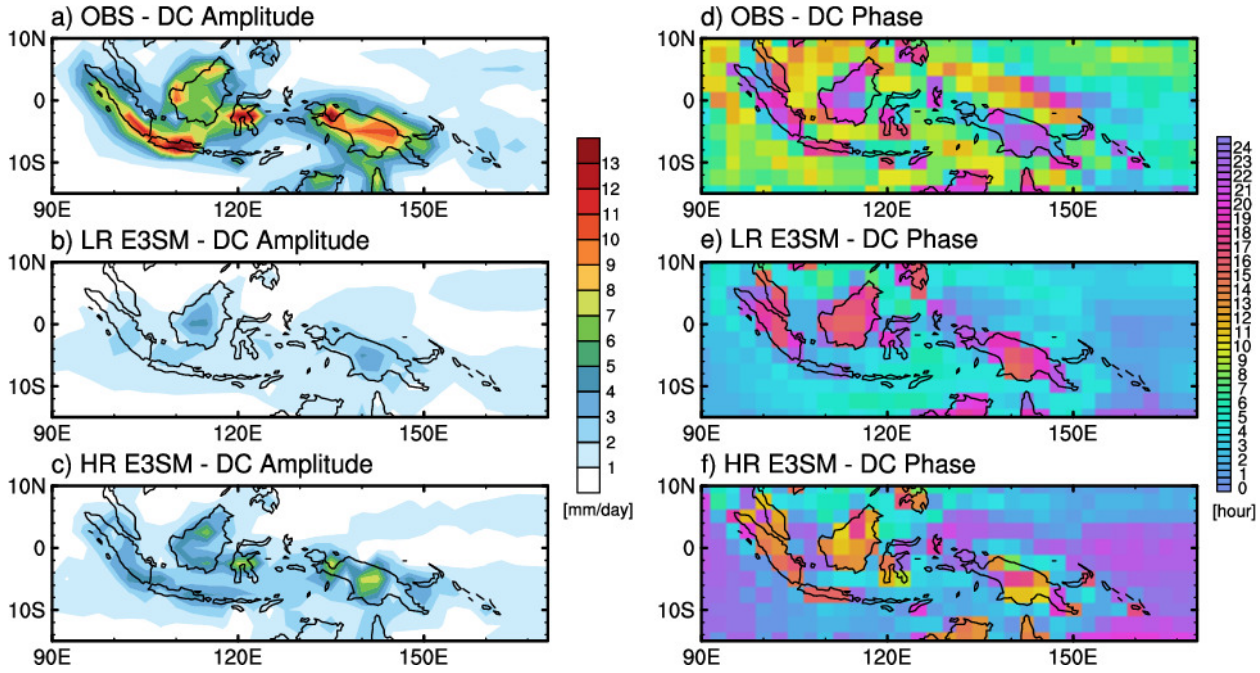

Figure 7. Climatological (left) amplitude (mm day^{-1}) and (right) phase (hour) of the diurnal harmonic of precipitation from (top) TRMM, (middle) LR E3SMv1, and (bottom) HR E3SMv1 during NDJFMA.

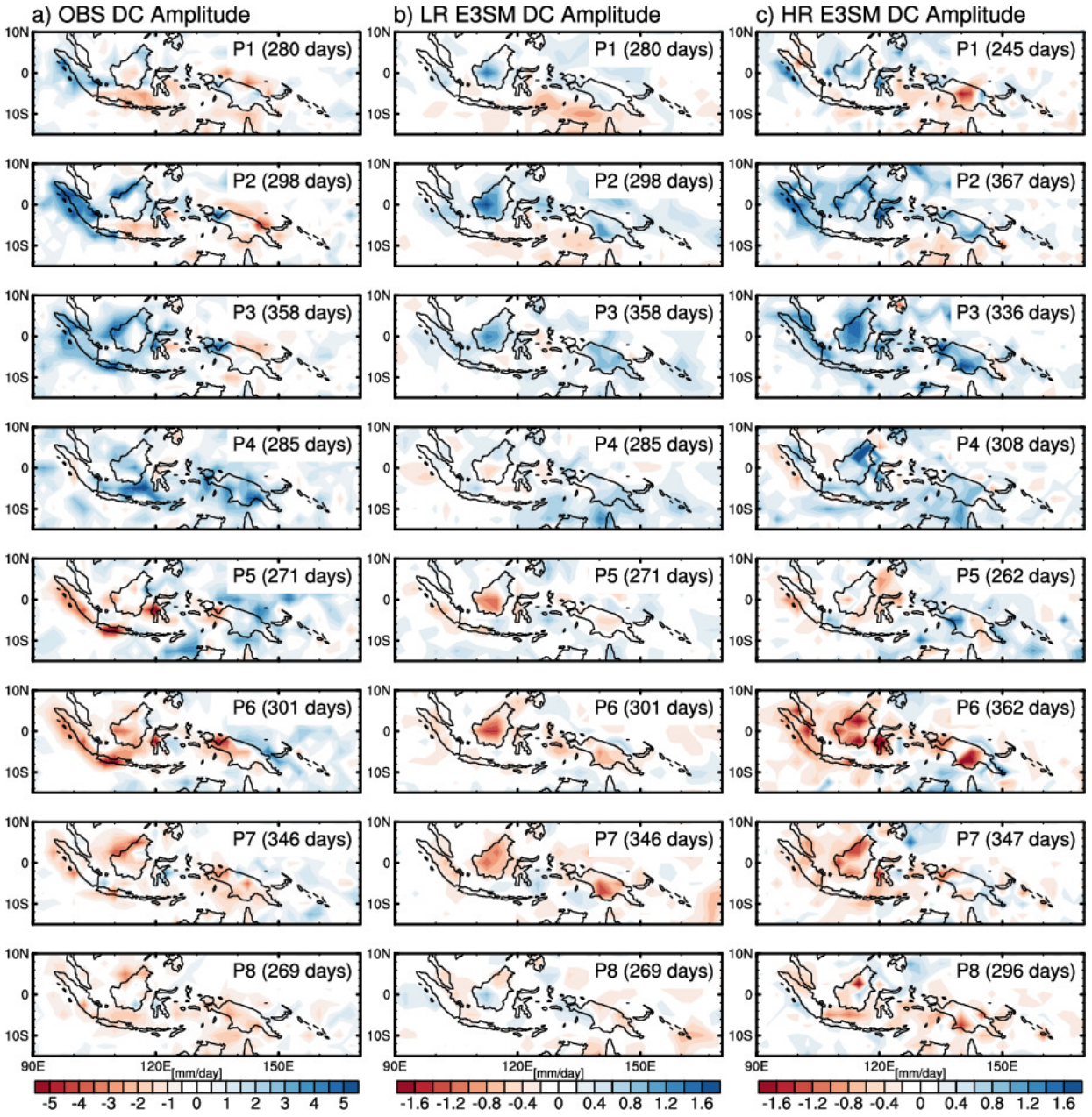

Figure 8. MJO life cycle composite maps of anomalous diurnal harmonic amplitude of precipitation (mm day^{-1}) obtained from each RMM phase during NDJFMA: a) TRMM, b) LR E3SMv1, and c) HR E3SMv1.

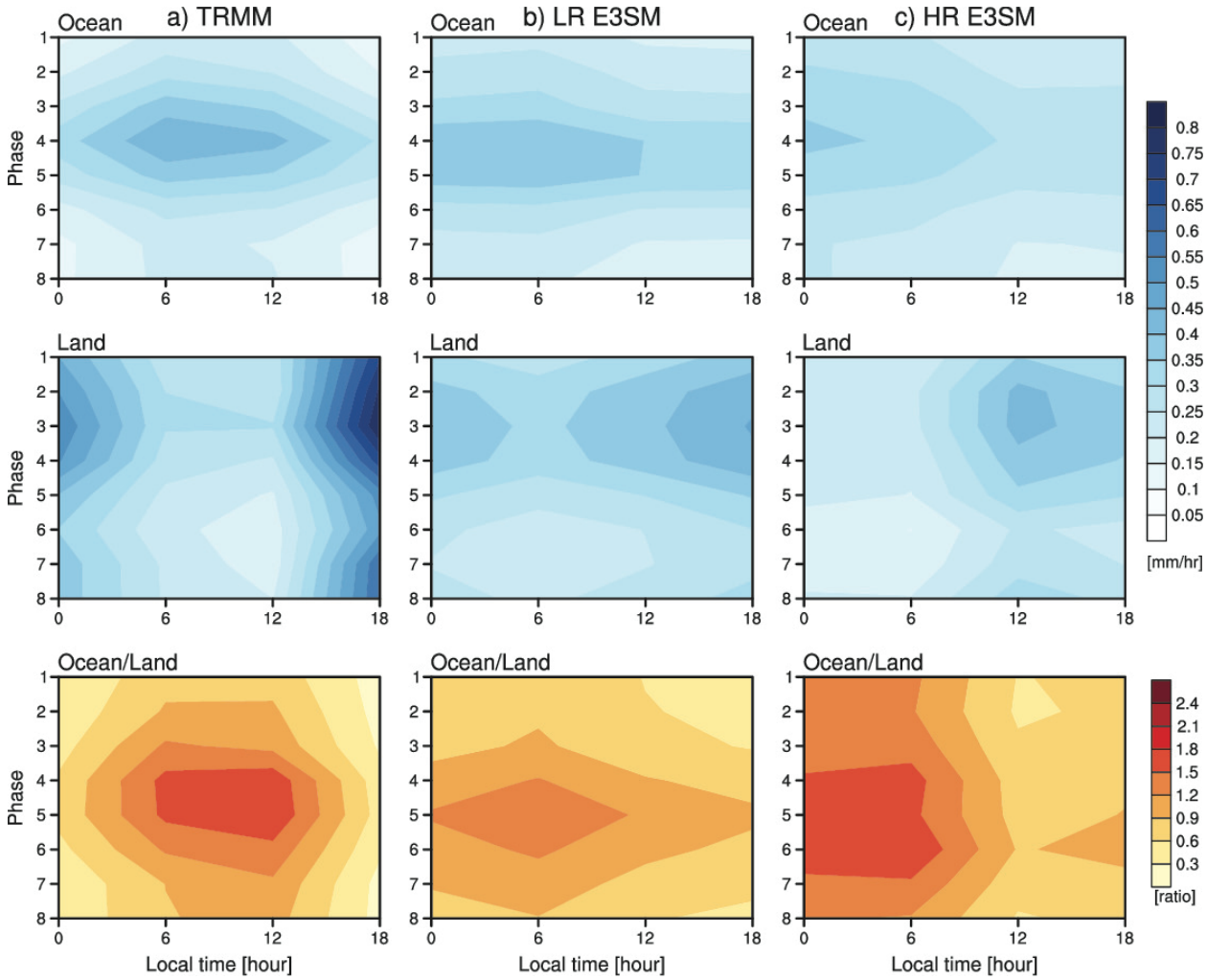

Figure 9. Composite diurnal cycle of (upper) oceanic and (middle) land precipitation (mm day^{-1}) and (lower) their ratio over the western Maritime Continent (15°S-10°N, 100-120°E) as a function of MJO phase: a) TRMM and b) LR E3SMv1, and c) HR E3SMv1.

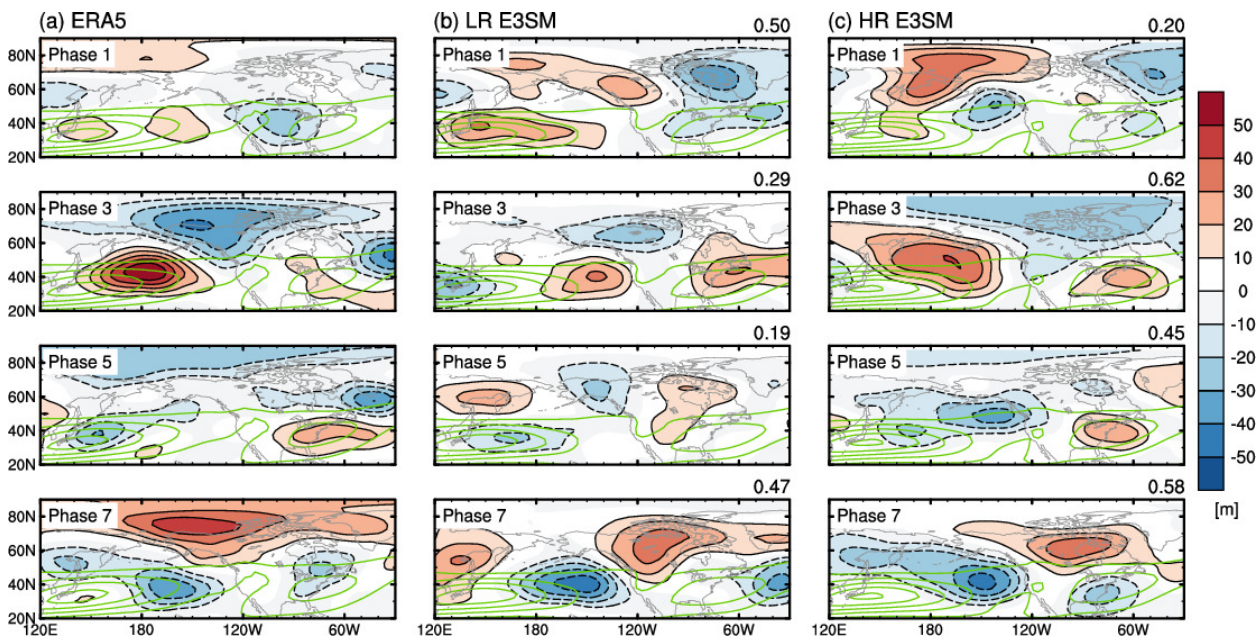

Figure 10. MJO life cycle composite maps of 5-9 days average 500-hPa geopotential height anomalies (m, shaded) obtained from the selected four RMM phases during NDJFMA. Green contours indicate the climatological 300-hPa zonal wind (m s^{-1}, contour interval: 10 m s^{-1}). Green contours begin from 20 m s^{-1}. a) ERA5, b) LR E3SMv1, and c) HR E3SMv1. For E3SM simulation results, the pattern correlation with the observed anomalies over the domain covered by the figures (20°-90°N, 120°-330°E) is indicated at the right top of each panel.

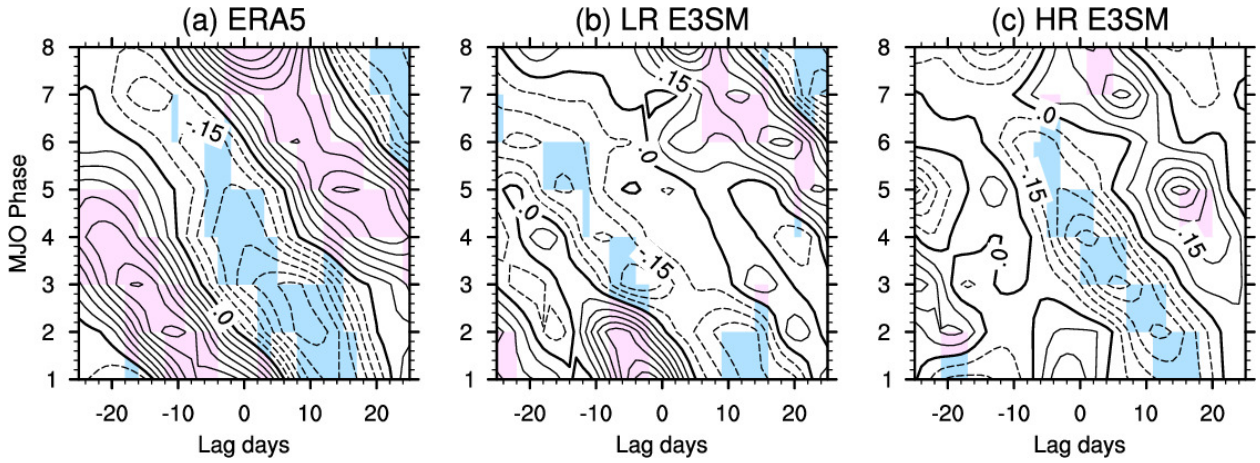

Figure 11. Lead-lag composite of the PNA index around strong MJO days for each MJO phase during NDJFMA: a) ERA5, b) LR E3SMv1, and c) HR E3SMv1. Pink and blue shading indicates that positive and negative composite values are statistically significant at the 95% confidence level.

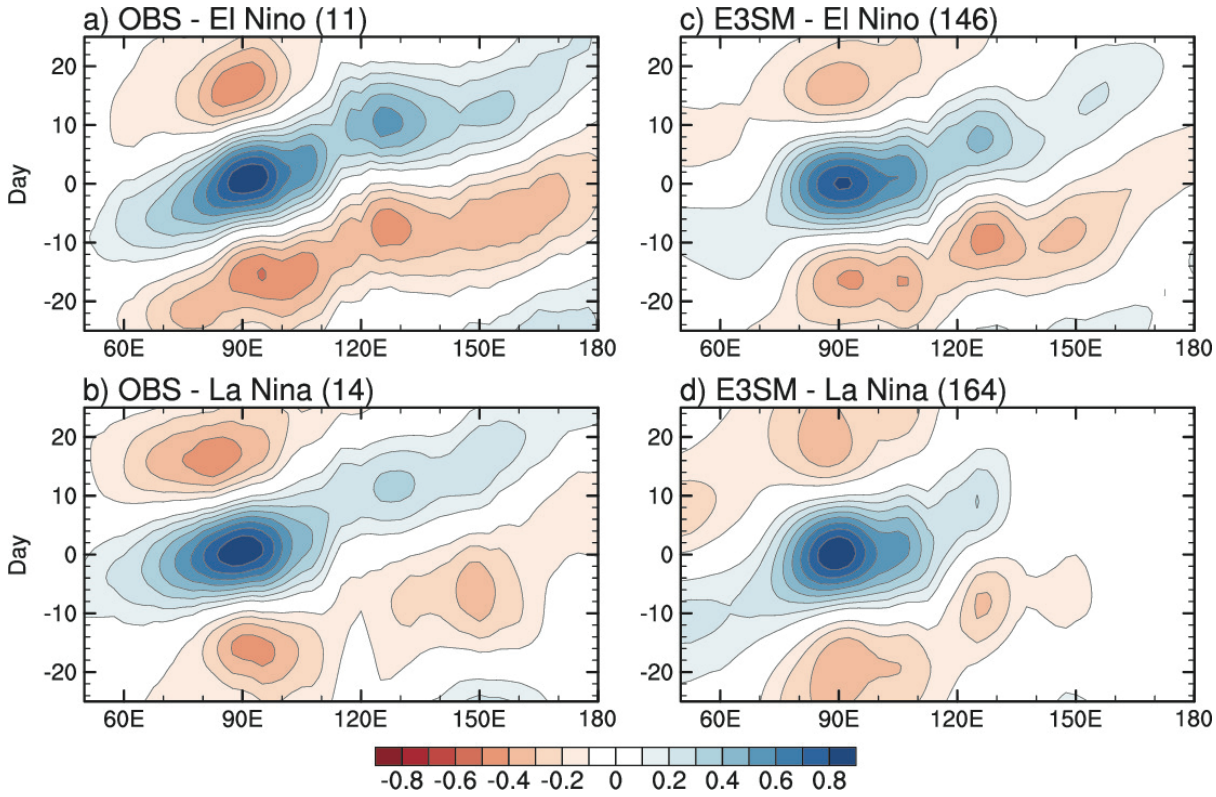

Figure 12. Longitude–lag diagram of equatorial (10°S–10°N) OLR regressed against intraseasonal OLR anomalies in the Indian Ocean reference region (5°S–5°N, 85–95°E) during DJF for the El Niño and La Niña years from (left) observations and (right) 5-ensemble CMIP6 Historical simulation made with LR E3SMv1. Numbers in parentheses denote the number El Niño and La Niña years. For observations and E3SMv1, El Niño and La Niña years are defined as the years with SST anomalies averaged over the Niño3.4 region (5°S–5°N, 170–120°W) being higher than its 0.5 standard deviation and lower than its -0.5 standard deviation, respectively.

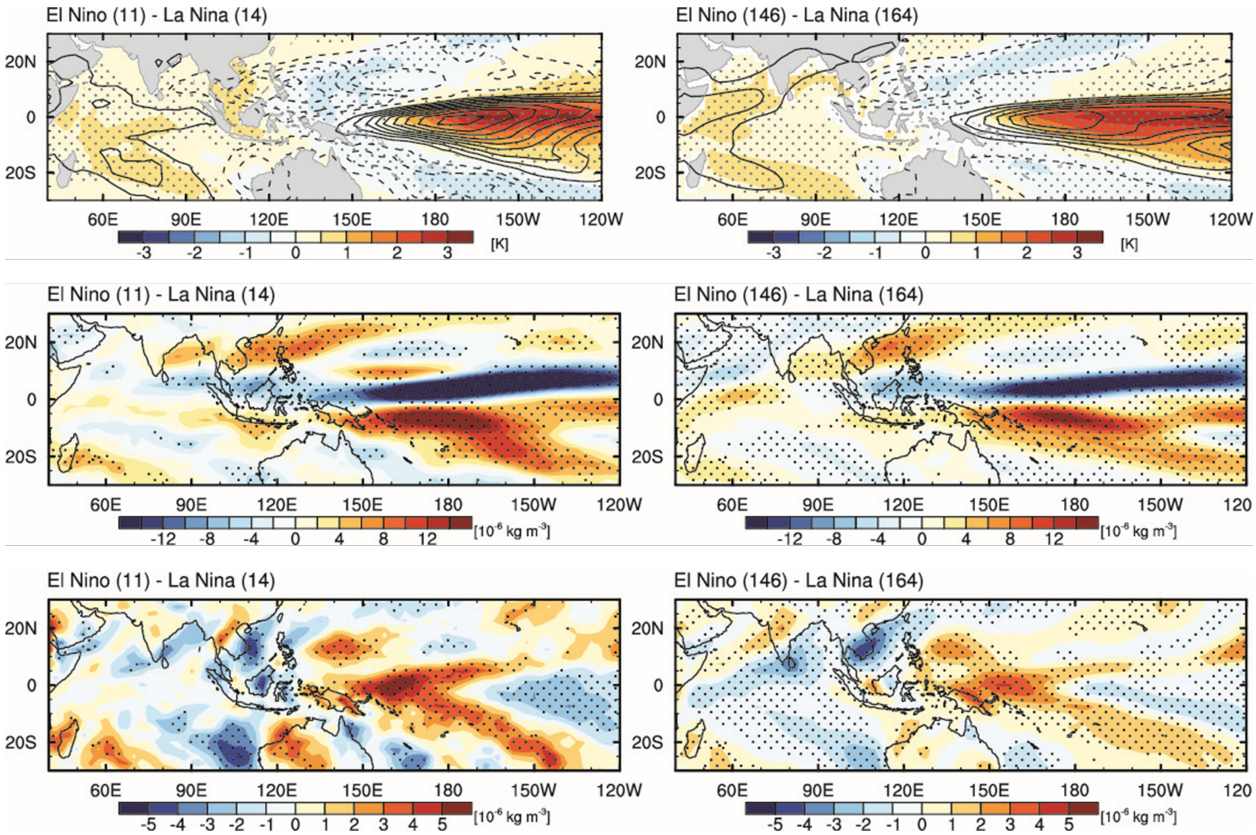

Figure 13. Differences between the El Niño and La Niña years in DJF mean state:(left) observations and (right) 5-ensemble CMIP6 Historical simulation made with LR E3SMv1. (top) SST (K, shaded) and precipitable water (kg m-2, contour), (middle) meridional and (bottom) zonal gradient of precipitable water (x 10^{-6} kg m^{-3}). Black dots indicate the differences are statistically significant at the 95% confidence level. Numbers in the parentheses denote the number of El Niño and La Niña years used in the analysis.

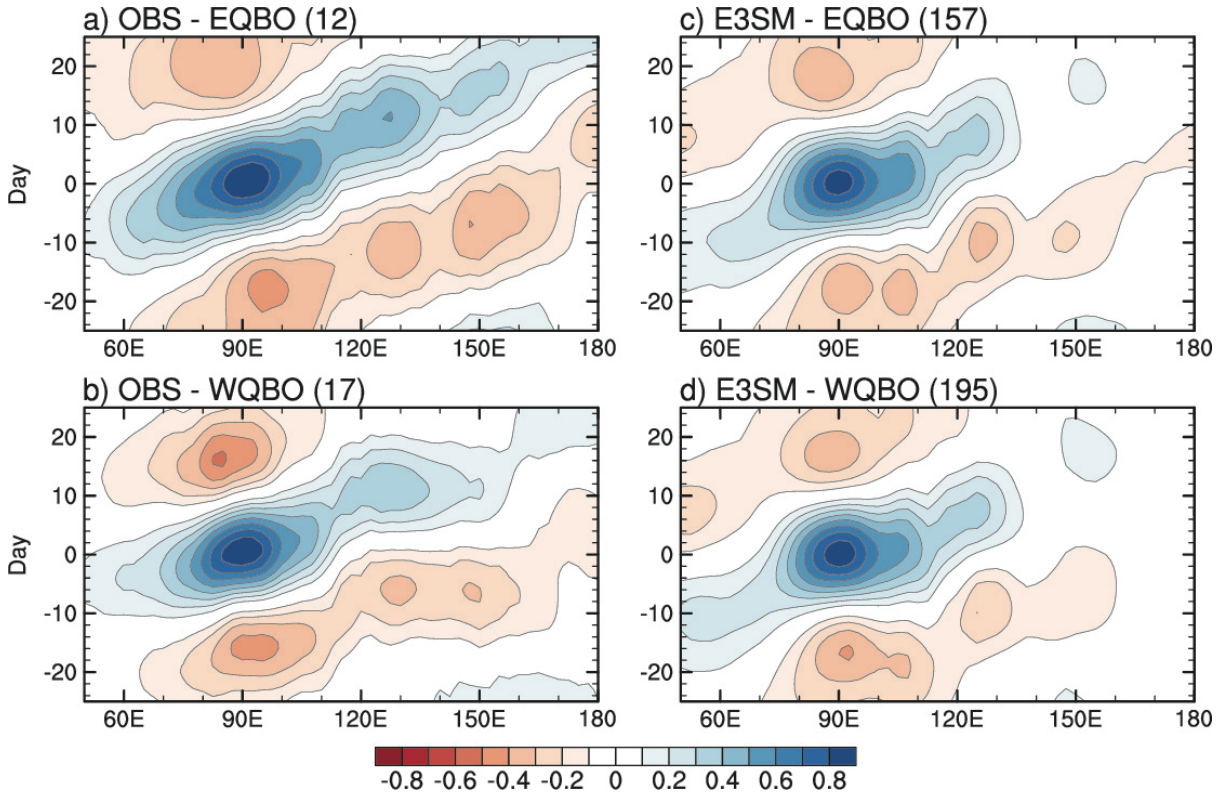

Figure 14. Same as Figure 12, except for the (top) EQBO and (bottom) WQBO years obtained as the years with 50-hPa zonal wind anomalies averaged in the equatorial band (10°S–10°N) being higher than 0.5 standard deviation and lower than -0.5 standard deviation, respectively.

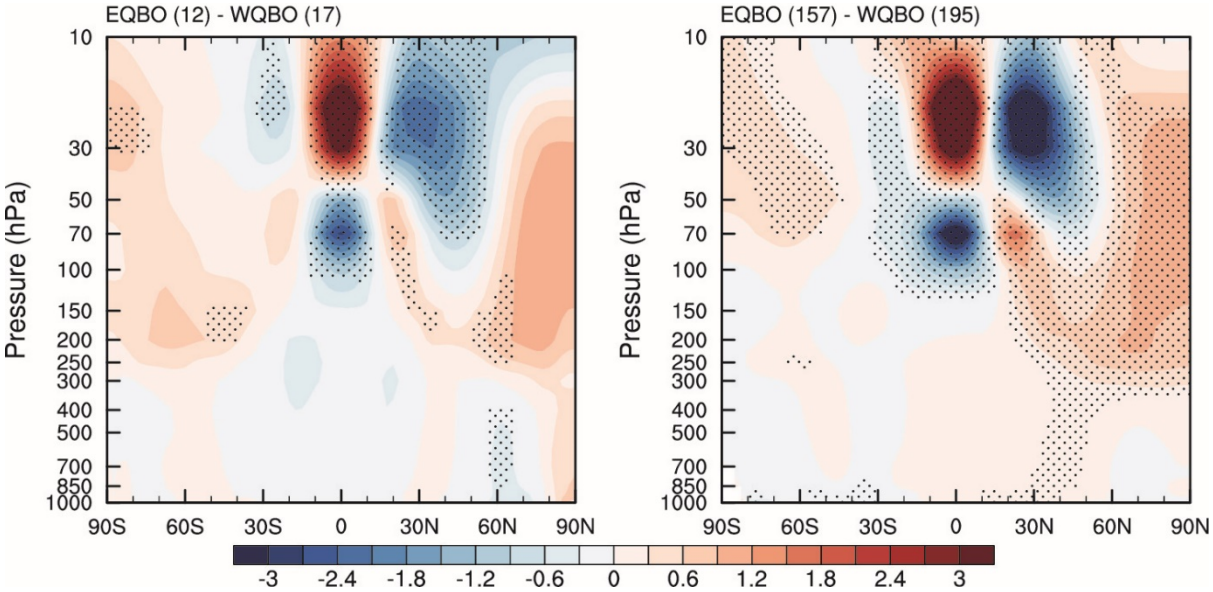

Figure 15. Differences between the EQBO and WQBO years in DJF-mean zonal-mean temperature (K): (left) observation and (right) 5-ensemble CMIP6 Historical simulation made with LR E3SMv1. Black dots indicate shaded differences are statistically significant at the 95% confidence level.

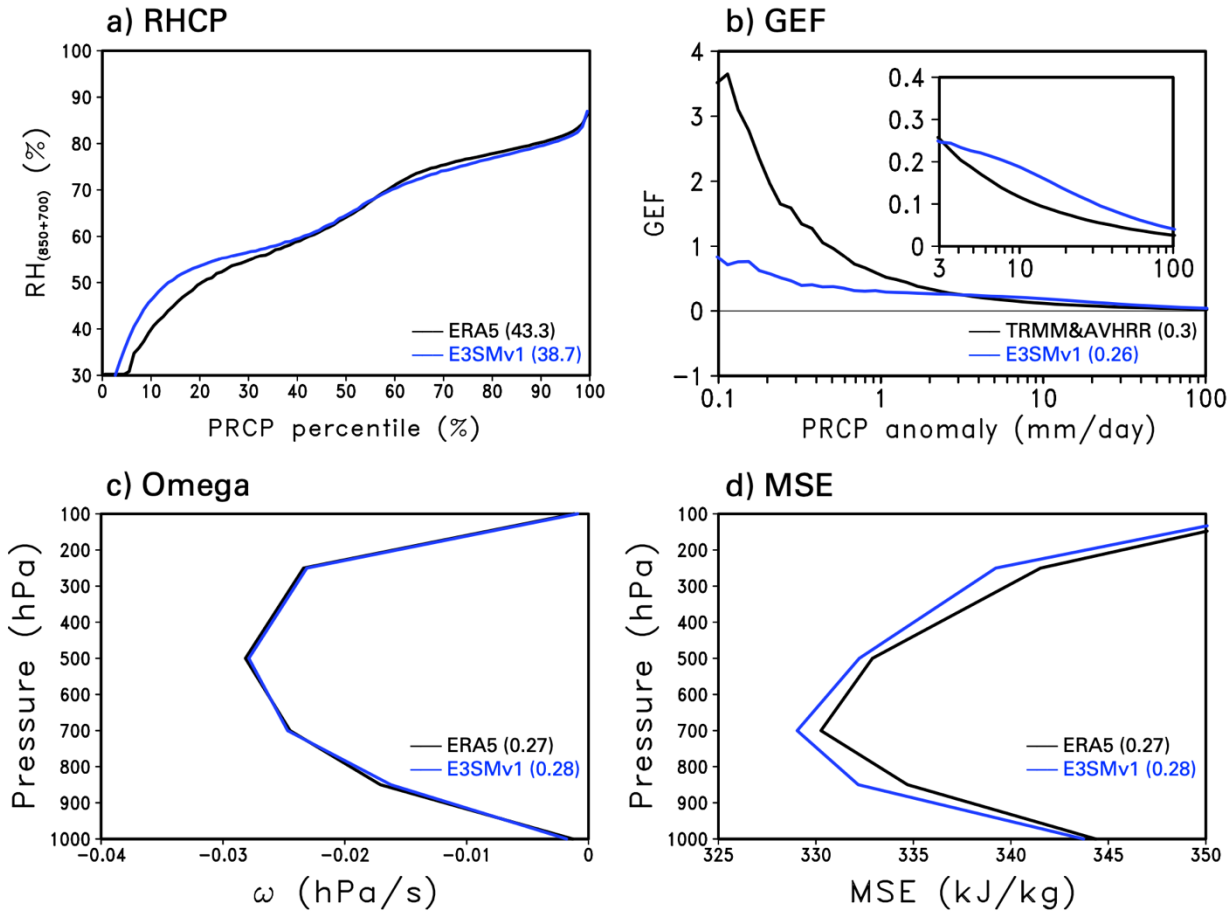

Figure 16. Process-oriented MJO diagnostics: a) the relative humidity composite based on precipitation percentile (RHCP, %), b) the greenhouse enhancement factor (GEF, unitless), and the vertical profiles of the mean state c) pressure velocity (hPa s^{-1}) and d) moist static energy (MSE, kJ kg^{-1}) from observations (black) and LR E3SMv1 (blue). The pressure velocity and MSE profiles are used for the calculation of normalized gross moist stability (NGMS). The Indo-Pacific warm pool area (60°E-180°E, 15°S-15°N) excluding land grid points is used for all the process-oriented diagnostics. Numbers in parentheses next to data labels denote the process-oriented metric values of RHCP, GEF, and NGMS.